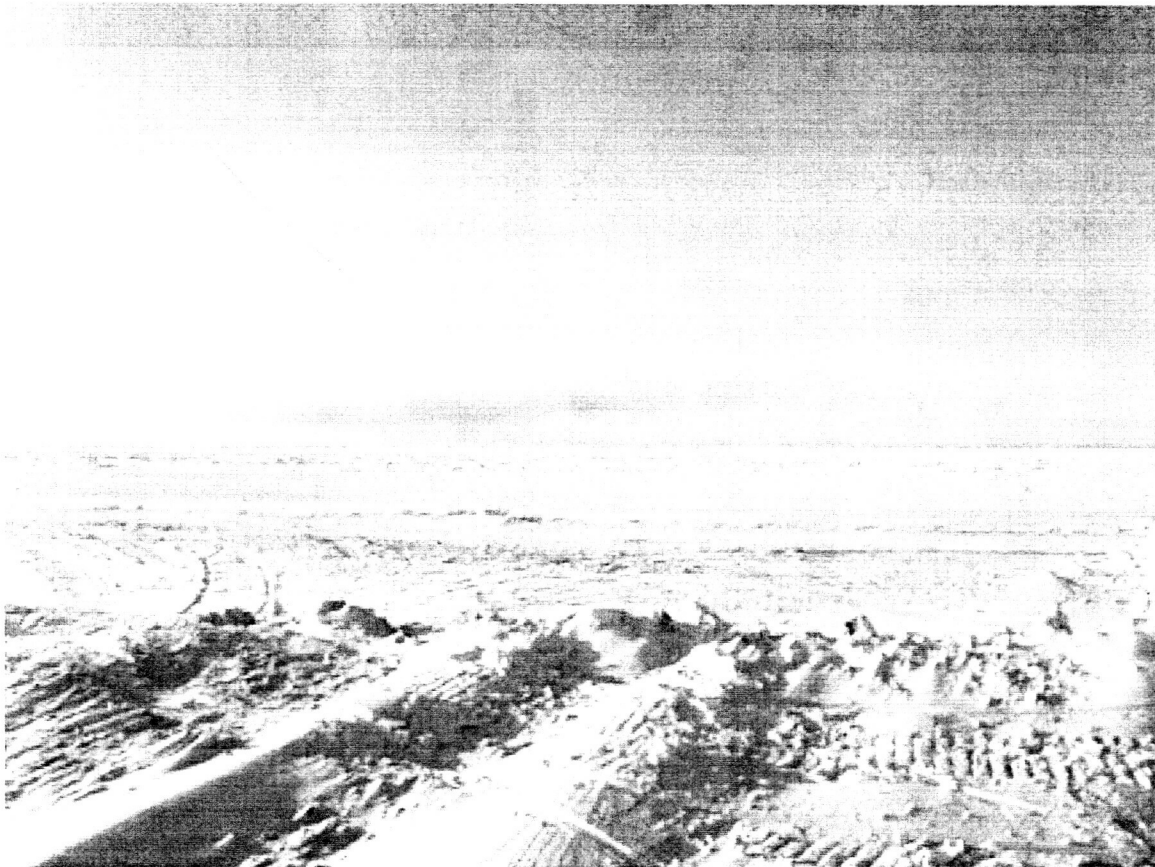# Improving the Simulation of Sea Ice Lead Conditions and Turbulent Fluxes Using RGPS Products and Merged RADARSAT, AVHRR and MODIS Data

Final Project Report to the National Aeronautics and Space Administration
Polar Research Program

Award No. NAG5-9861

Principal Investigator:

James A. Maslanik
University of Colorado
Colorado Center for Astrodynamics Research
Campus Box 431
Boulder, CO 80309-0431
Email: james.maslanik@colorado.edu
303-492-9874

Table of Contents

Cover Photograph: Moisture plumes rising from a flaw lead offshore of Barrow, Alaska in March 2003.

1.0 Project Overview

1.1 Background

The importance of sea ice leads in the ice-ocean-atmosphere system as illustrated in Figure 1 lies in the fact that each of the boxes in the "surface processes" interface in this diagram is closely linked to lead conditions. For example, heat, moisture and salt exchange between the ocean and atmosphere within the ice pack occur nearly entirely through leads. The shear, divergence and convergence associated with lead formation and closure alter surface and basal roughness and topography, which in turn affects momentum transfer in the atmosphere and ocean boundary layers, and modifies the accumulation of snow on the ice surface, which then affects heat conduction and summertime albedo. In addition to providing openings for loss of heat and moisture fluxes to the atmosphere, leads absorb solar energy, which is used to melt ice and is transmitting to the underlying ocean. Given that leads dominate the ice-ocean interface in this manner, then it stands to reason that focusing on lead treatments within models can identify performance limitations of models and yield routes for significant improvements.
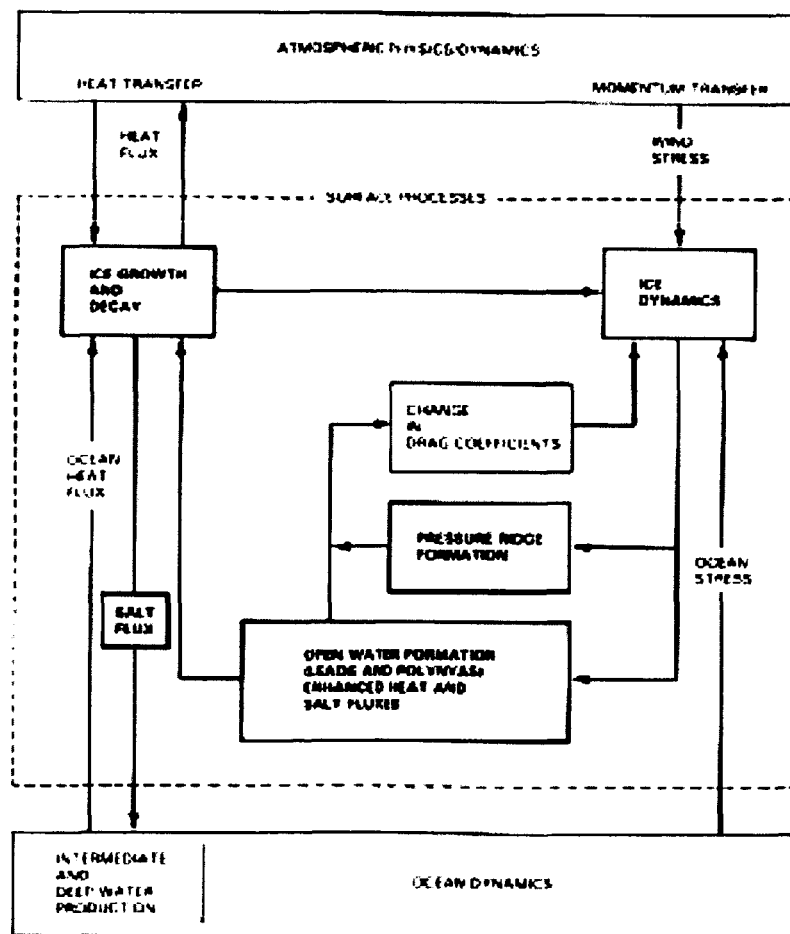

Figure 1. A system model for winter sea ice behavior (adapted from Butler et al. 1987).

Figures 2-4 illustrate some of the key aspects of leads that form the foundation of this project. In Figure 2, large plumes of moisture can be seen rising from a lead located near Barrow, Alaska. Note the stream of cloud that is drifting downwind, formed from this moisture source. This type of heat and moisture transfer to the atmosphere occurs primarily when the lead consists of some open water. Upon the formation of an ice cover, the heat and moisture exchange is greatly reduced.

Figure 2. Plumes of moisture rising from an open lead near Barrow, Alaska during a cold period with relatively calm winds – conditions that favor development of such plumes. Leads such as this one as well as the more common smaller leads are a key source of heat and moisture for the atmospheric boundary layer. In this case, a stream of cloud resulting from the plumes can be seen drifting downwind.

In all climate models to date, leads are treated either as entirely open water (a situation that is very rare in winter when heat and moisture fluxes are greatest) or entirely covered by a new layer of ice. In fact, nearly all leads lie somewhere between these extremes (e.g., Figure 3), with a portion of the lead covered by ice while winds maintain some open water (typical of "frazil ice" leads) or the lead entirely frozen over with an ice layer ("congelation ice" leads [e.g., Figure 4]). In our earlier work, we showed via various model calculations that how a lead is treated in this regard – entirely open water, entirely ice covered, or an in-between situation – makes a substantial difference in the calculated fluxes, and thus differences in boundary layer conditions and formation of new ice.

Figure 3. A sea ice lead with varying thicknesses of new ice formation and with some open water, illustrating the contrast between actual leads compared to their simplified treatment as 100% open water or 100% ice covered within climate models.

Figure 4. A narrower lead typical of smaller "congelation ice" leads.

As climate models improve, primarily through the ability to better treat the details of surface and atmospheric boundary layer conditions such as those represented in the discussion above, the typical treatment of lead processes in turn need to be refined to reflect the fact that factors such as lead width, orientation, and wind speed influence the types and rates re-freezing of leads, and thus the rate and total amount of heat and moisture transfer between the ocean and atmosphere. Lead models now exist that treat these conditions explicitly and which therefore provide much-improved flux estimates. These models or similar versions can potentially be adapted for use within climate simulations. Standing in the way of this advance is the need to be able provide the additional details regarding lead conditions that these models need based on conditions simulated by the climate model (for example, lead width distributions and lead orientations as a function of ice motion, ice characteristics and wind direction). Recently, remotely sensed data such as RADARSAT imagery, a long time series of AVHRR data, and the suite of products from the Terra platform have become available that, when used in conjunction with aircraft and field data and detailed process models, should allow the development of relationships and parameterizations suitable for improving the treatment of lead processes within large-scale models.

1.2 Objectives

The premise of our project was that modeling and remote sensing of sea ice processes have reached a level of maturity where the models require detailed information for testing and refinements, and where such information can now be obtained from multisensor approaches. Given this, the goals of our work were to: (a) refine and test the local-scale parameterizations used within an existing, detailed lead model; (b) identify relationships between the local-scale lead characteristics needed as input to the lead model and large-scale sea ice conditions that can be simulated by climate models; and (c) test the improvement in the climate simulations when these relationships are used to implement the detailed lead flux calculations. A key aspect of the project was the use of RADARSAT data, in concert with a wide range of other data types, to document fine-through coarse-scale characteristics of leads in the context of the types of background ice and atmospheric information that can be simulated by state-of-the-art coupled ice-atmosphere-ocean models such as the Arctic Regional Climate System Model (ARCSyM). Objectives to meet these goals included:

- Derivation of detailed lead conditions for modeling test cases using RADARSAT, aircraft, and other satellite data sets acquired the Surface Heat Budget of the Arctic (SHEBA) period, with additional test cases during the expected RADARSAT/MODIS overlap period in autumn, 2000;
- Use of these data to evaluate the differences in fluxes and ice growth for leads estimated using a new lead model versus estimates obtained using standard bulk formulae;
- Applications of the SAR data and SAR-based products to test and refine the parameterizations and assumptions inherent to the new lead model;
- Identify correlations and relationships between local lead conditions critical for the lead model and larger-scale ice and atmospheric conditions;

6

- Link these correlations to conditions simulated by large-scale models;
- Demonstrate the improvement achieved by implementing these remote-sensing derived parameterizations within an Arctic climate simulation.
- Carry out a limited comparison of the Arctic-based parameterizations with Antarctic ice conditions to assess how representative such parameterizations are likely to be Southern Ocean simulations.

1.3 Methodology

Figure 5 diagrams the main components of the project and illustrates the linkages between remote sensing and modeling. The main outputs to be generated are highlighted in bold italics. The bulk of the project activities focused on (a) identification and assembly of multisensor data sets depicting various lead conditions, (b) development and testing of lead processes and parameterizations within the detailed lead model and within a stand-alone ice model destined for use in ARCSyM, and (c) initial studies of relationships between lead characteristics and large scale atmospheric and weather conditions. .
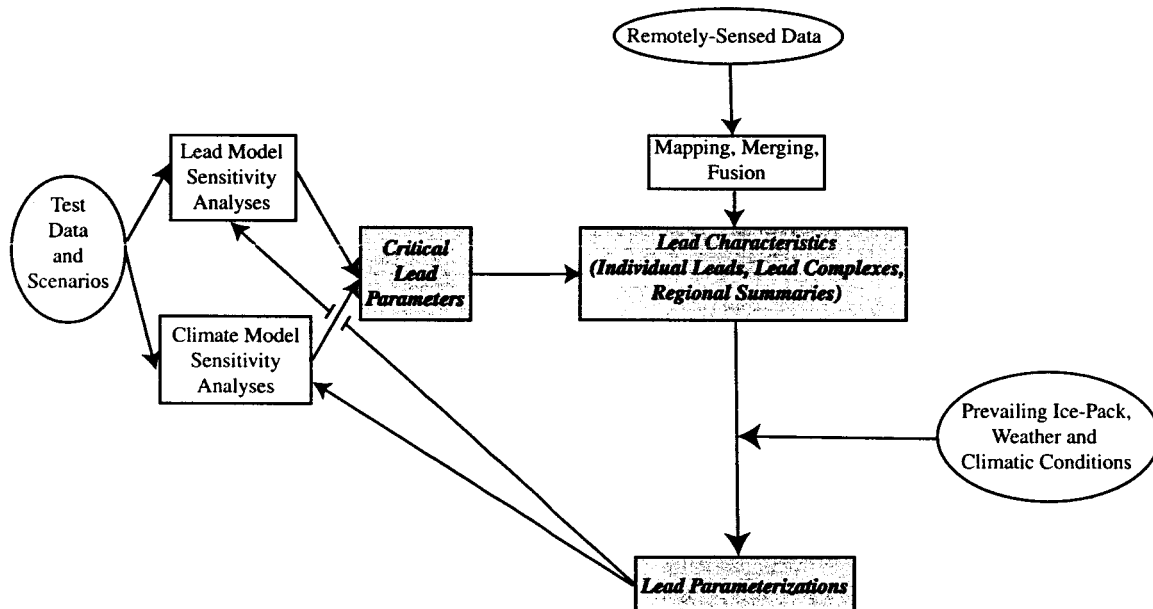
Figure 5. Flow diagram illustrating the main project components. Inputs and data sets are enclosed within ovals. Key outputs are indicated by the shaded boxes.

The sequence of steps shown in Figure 5 to derive lead characteristics involves a variety of scales and data sets (Figure 6). On local scales, high resolution data are used to map conditions associated with individual leads. Lower resolution imagery that provide larger areal coverages yield information on basic characteristics of lead groupings (lead complexes). Analysis of this local-scale and lead-complex information in the context of general weather, ice-pack and climatic conditions then should provide the basis for parameterizations that relate detailed lead properties to general conditions that can be simulated within climate models.

7

Parameters   *Scale*   *Source*

Width
Orientation   ◄────── Individual Leads ◄──────── Aircraft data
Surface Characteristics   NTM imagery
                                                                     LandSat/ASTER
                                                                     RADARSAT
                                                                     MODIS

Lead Characteristics   RADARSAT
(width, etc.) Summarized   ◄────── Lead Complexes ◄────────── MODIS
over Regions   AVHRR

Characteristics of
Complexes in   RADARSAT
Relation to   ◄────── Context within Ice Pack ◄── MODIS
Ice Thickness, Type,   SSM/I
and Deformation   RGPS Products

Lead Complexes in   NCEP
Relation to Winds,   ◄────── Context within Large-Scale ◄── IABP
Drift, Temperature,   Atmospheric Conditions   POLES
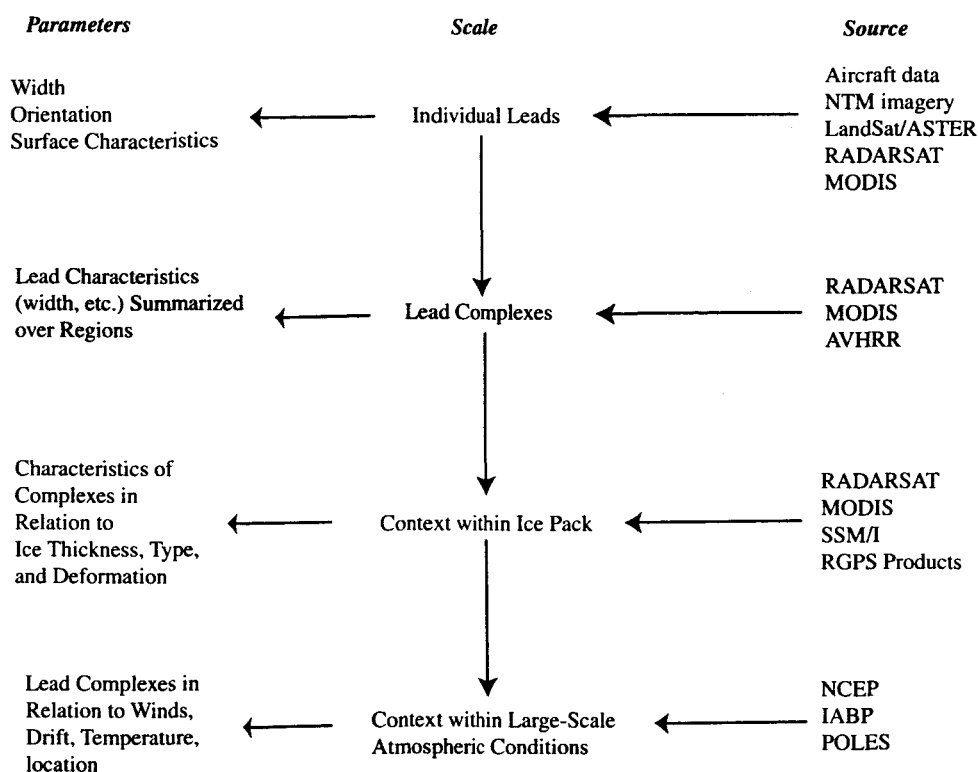location

Figure 6. Schematic of the relationships between data and information ("Source"), scale of lead features and lead groupings ("Scale") and the derived output parameters ("Parameters").

2.0 Executive Summary

With this background in hand, the following sections describe the main project tasks and results. A summary of our main activities and findings is given below, followed by additional discussion of main project elements. During this three-year effort, we addressed each of the objectives listed above, with the exception of the climate model simulations. While we carried out some work to plan how the flux-related improvements might be best incorporated into climate models, we did not have time to implement new code and perform new simulations. Nevertheless, our work does provide the basis for doing so, and carrying these results forward to do experiments with models such as NCAR's community sea ice model, a coupled regional model such as ARCSyM, or a full GCM such as the CSM is very feasible. We hope to do so as part as further research efforts.

The major (in terms of science results and effort) activities and findings during the project are as follows:

- Investigated a series of AVHRR, MODIS, RADARSAT and AMSR-E image time series to identify large-scale lead patterns.

- Obtained and georeferenced a combined set of SAR, AVHRR, and MODIS for the southern and central Beaufort Sea and the eastern Chukchi Sea.
- Acquired and re-gridded NCEP forcing fields useful for quantifying relationships between atmospheric forcings and lead patterns.
- Generated a similar data set for ice motion, including updates and refinements of AVHRR Polar Pathfinder ice motion fields.
- Used ice concentration and ice motion data to calculate ice residence times (i.e., ice age) for the Arctic and Antarctic and related these ages to lead formation and characteristics.
- Demonstrated that the distribution of ice ages in the Arctic Basin has changed substantially over the last 22 years, with a large decrease in the area of oldest ice.
- Tested a suite of MATLAB software tools for data fusion.
- Tested fusion methods provided by the PCI Geomatica software package.
- Explored data fusion approaches applied composites of AVHRR, MODIS and RADARSAT imagery to extract lead information based on combined optical, thermal and radar characteristics.
- Tested and applied image classifications (maximum likelihood) and data visualization as data fusion approaches as means of extracting a variety of lead parameters.
- Quantified effects of image type and spatial resolution on retrieved lead fractions and conditions.
- Employed a set of software routines to extract "object oriented" lead information such as width, length and orientation useful for comparing to large-scale forcing fields.
- Modified and applied a lead flux model to quantify effects of different input information, lead parameterizations, and transfer-coefficient treatments on turbulent fluxe estimates.
- Tested additional lead flux models capable of providing improved flux calculations given the types of lead information provided by the fusion, classification and object characterization steps listed above.
- Used ice motion fields at various scales to quantify the formation of open water via calculation of "synthetic leads".
- Through the synthetic lead analysis, showed that even in cases of net convergence (i.e., areas where an ice model would produce no open water), RADARSAT-derived ice motion yields some open water production due to the apparent plate-like nature of the ice pack at this fine spatial scale.

In general, we found that our investigations took us down many different paths, yielding useful insights and setting the stage for follow-on work. We were not as successful as we would have liked in terms of delving deeply into any one of these areas though, and underestimated the level of effort needed to assemble sufficient data sets to yield reliable statistical results. Another year of work would probably be needed to achieve the full set of goals that we set out for ourselves in the original proposal. The synthetic lead analysis and the subsequent discovery using the RADARSAT data that models are likely to underestimate open water production is a key finding. The calculation of motions at different scales, combined with other information on ice conditions such as thickness and ice type/age would, we believe, provide the means of parameterizing this additional open

water production in climate models. This could yield substantial changes in ice model performance and predictions and thus warrants pursuing with additional research.

3.0 Activities and Findings

3.1 Data Sets

Considerable effort was expended in each year of the project to assemble sets of data for the different scales indicated in Figure 6. To draw inferences across these scales requires that the various data sets sample ice conditions as coincident as possible in time and space. The data sets that have been assembled to support our analyses include:

- A suite of data for 20-22 May 1998 in the SHEBA area. The data include high resolution video, passive microwave (Airborne Microwave Imaging Rdiometer [AIMR]), multispectral optical imagery and thermal profiling data from the NCAR C-130, MODIS Airborne Simulator (MAS) data from the NASA ER-2, a National Technical Means satellite image (obtained from NSIDC) (all acquired on 20 May), and RADARSAT imagery (acquired on 21 and 22 May and obtained from the SHEBA project [courtesy Dr. Harry Stern] and ASF) and Polar Pathfinder calibrated AVHRR channels and derived products.
- in-situ lead observations, C-130 products, and RADARSAT imagery corresponding to development of new leads in the SHEBA ship vicinity.
- Lead statistics derived from C-130 AIMR data for SHEBA.
- RADARSAT and AVHRR sequences of lead opening and re-freezing events during December 1997 - January 1998 in the SHEBA area, along with RGPS products for this period. (SAR and AVHRR are available for the full SHEBA period {November 1997 - October 1998], but we are focusing on the significant deformation that occurred during the mid-winter period.)
- RADARSAT, MODIS, and AVHRR coverages of a large lead complex (also visible in SSM/I data) in the Beaufort Sea in March 2000.
- RADARSAT, AVHRR, and Aerosonde unmanned aerial vehicle (UAV) images of near-shore leads in the Barrow, Alaska area in April, 2001.
- RADARSAT, AVHRR, MODIS and AMSR-E satellite imagery along with aircraft imagery from the NASA P-3 for the Beaufort, Chukchi and Bering seas as supplied by the AMSR-E ice products validation effort.

Various examples of these various data set combinations and resulting analyses are given below. Please note that all RADARSAT and AMSR-E data are courtesy of RADARSAT International (RSI) and JAXA, respectively.

3.2 RADARSAT and AVHRR Combinations

An example of combinations of SAR (backscatter) and AVHRR (skin temperature) is shown in Figure 7. In this example, the merging of backscatter and skin temperature is used to infer the area of recently-opened leads that is most likely to consist of open water or new ice. Comparison of these estimates to open water and new ice production

estimated by the RGPS should provide insight into the relationships between ice motion and lead surface properties. The fusion of the SAR and skin temperature data also allows assignment of physical temperatures to the different ice types. In this case, mean skin temperature for the high-backscatter old ice is 238 K. Lead ice temperatures average 250 K.

In the context of the larger region in the Beaufort and Chukchi seas, the leads in Figure 7 can be seen to be part of a more extensive network of leads covering much of the area (Figure 8). These leads developed under the influence of a strong high pressure system centered in the Chukchi Sea, with low pressure over the Canadian Archipelago in early through mid December, with the leads oriented approximately perpendicular to the surface winds. The particular lead opening event depicted in Figure 7 occurred during a period of relatively weak winds, when the leads that had formed earlier in the month

Radarsat backscatter

AVHRR Polar Pathfinder skin temperature

Composite of backscatter and skin temperature (blue tones = high backscatter, low skin temperature; red tones = low backscatter, high temperature; yellow tones = high backscatter, high temperature; purple tones = intermediate backscatter, intermediate temperature)

Image classification based on backscatter and skin temperature thresholds. Blue pixels are probable open water areas (low backscatter and high temperature). Red areas are probable new ice (intermediate to high backscatter and high temperature)

Figure 7. Co-registered RADARSAT backscatter and AVHRR skin temperature scenes, false-color composite and combined backscatter/skin temperature classification of open water and new ice for the SHEBA area on 25 December 1997. (RADARSAT data courtesy of RSI, Inc.)

11

reopened. This opening of leads during slack winds following periods of sustained strong winds appears to be typical of the SHEBA period. This linkage between observed lead conditions and atmospheric forcing is the type of observation needed to provide parameterizations of detailed lead conditions such as the precise timing and nature of lead characteristics in relation to large-scale forcings simulated within models.
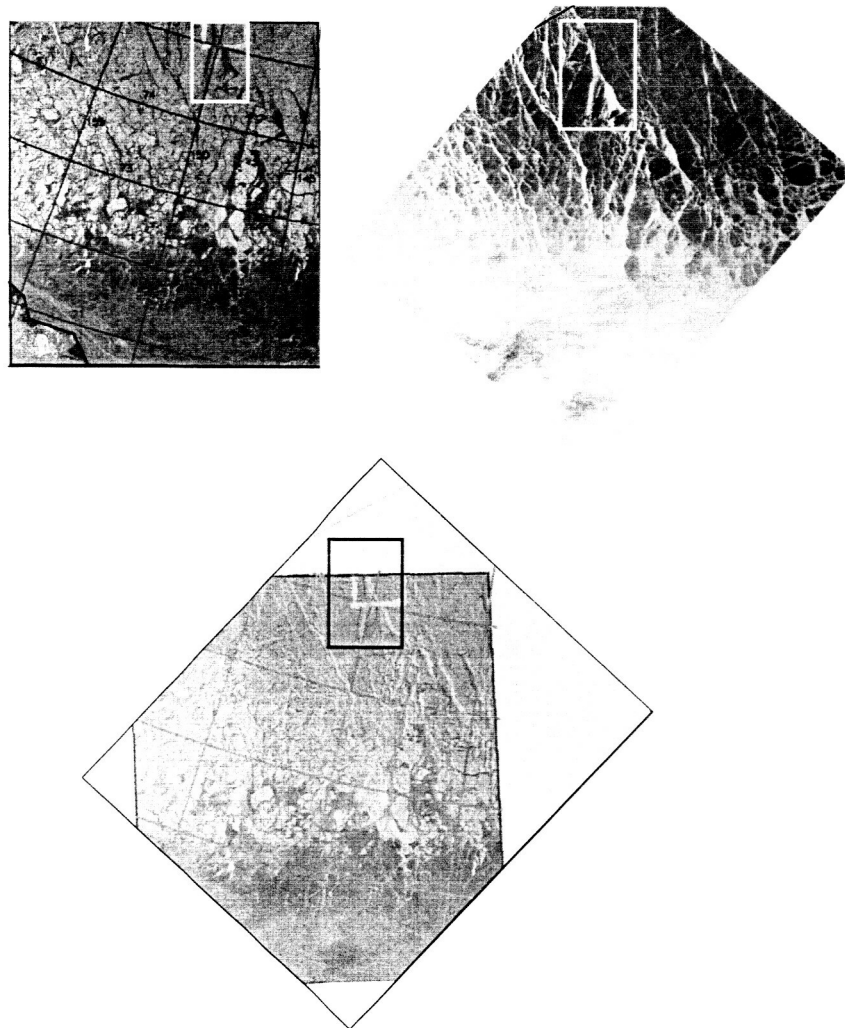

Figure 8. Fusion of reduced-resolution RADARSAT ScanSAR and AVHRR skin temperature images for 25 Dec. 1997 for a larger portion of the Beaufort and Chukchi seas. The sub-region shown earlier in Figure 7 is enclosed in the white and black boxes. (RADARSAT data courtesy of RSI, Inc.).

12

3.3 Lead Identification and Classification in Multisensor Imagery

3.3.1 Threshold Classification of Coincident Imagery

The images from the previous section were classified into ice/no ice classes using various thresholds for the different frequencies and sensors. A purely subjective visual approach was used to create the lead masks for the various images. Thresholds were arbitrary chosen until a particular value produced the desired mask. To establish a common area, the AVHRR and MODIS data sets were subset to only include pixels present in the SAR imagery. When the thresholding was complete, it became clear that it was difficult to produce masks which were uniform across the various frequencies. For instance, the acceptable mask for the AVHRR surface temperature image (Figure 9a) has a different distribution of lead pixels than did the AVHRR albedo lead mask (Figure 9b). This is due to the false identification of lead pixels (such as due to cloud contamination in the upper left) or the non identification of lead pixels that is inherent with single channel thresholding classifications. This discrepancy becomes even more evident when thresholding is applied to the SAR imagery (Figure 9c). A more integrated approach to lead classification would be one which combined information from different sensors and frequencies. The maximum likelihood classification described in the next section is one such approach.
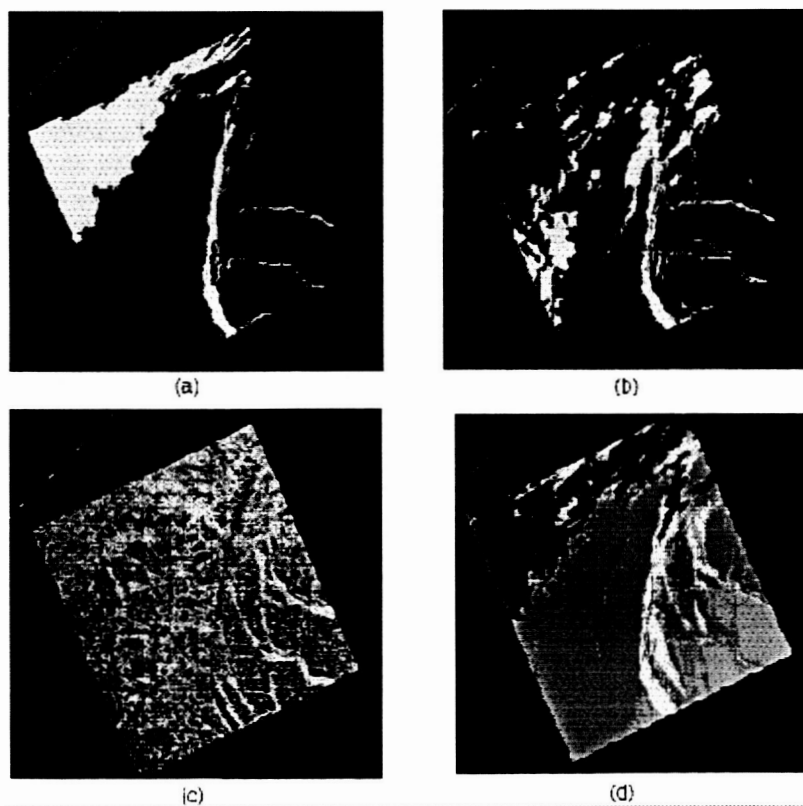

Figure 9. Threshold-based lead classification applied to AVHRR skin temperatures (a), AVHRR broadband albedo (b), SAR backscatter (c). Maximum likelihood classification using AVHRR albedo, AVHRR temperature, and SAR radar backscatter, yielding five classes (d).

13

3.3.2 Multisensor Analyses of Lead Complexes

We developed an approach for combining multiple data sets to further define relationships between local ice conditions and parameters such as pressure fields, winds, ice drift and ice age that can be simulated by models. The procedure is illustrated in Figure 10. This example is taken from a sequence of comparisons underway between lead
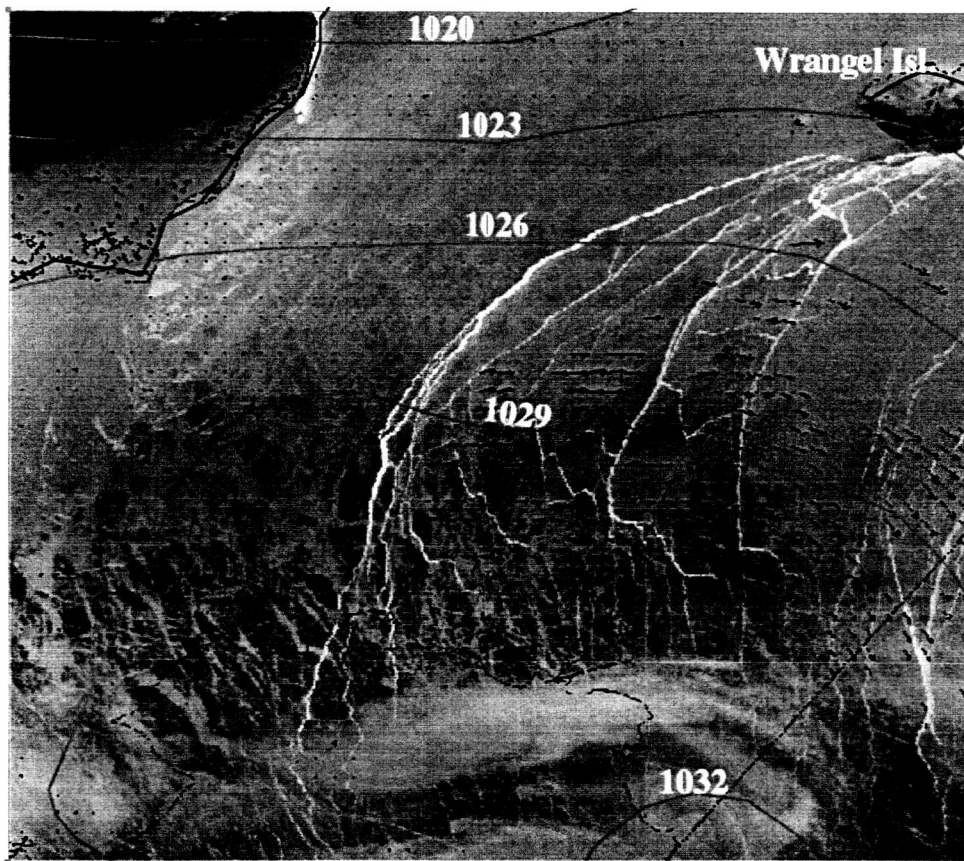

Figure 10. An example from the SHEBA sequence of AVHRR skin temperatures, NCEP sea level pressure data (red contours), and AVHRR-derived ice motion (black arrows) for February 18, 1998. The SHEBA camp location is indicated by the red square. The full SHEBA drift track is shown in blue. Note the extensive lead patterns, orientation relative to the geostrophic winds and ice motion, and the changes in lead patterns between the first-year ice pack (warmer/lighter gray area) versus the predominantly multiyear pack (colder/darker gray)

patterns and ice drift. In this case, a large and extensive lead complex has opened across the Beaufort and Chuckchi seas in conjunction with winds from the west-southwest associated with a strong high pressure system centered at about 80 degrees north, 150

14

degrees west. Of particular interest in these image sequences are factors such as lead width, length, and orientation, which affect turbulent fluxes through changes in fetch and variations in ice surface characteristics. In Figure 10, for example, the leads are wide and nearly continuous within the first-year ice pack, but the lead patterns change within the multiyear ice pack (the darker, i.e., colder, portion of the pack in Figure 10, which also conforms to the multiyear ice cover shown in SSM/I data and in NIC charts). Ice motion in the region in Figure 10 can be seen in the context of the broader-scale SSM/I-derived motion patterns (not shown). In this case, the leads in the central portion of the ice pack are oriented nearly perpendicular to the ice motion, while the long, continuous leads in the first-year pack are aligned at about a 45 degree angle to the motions. Figure 11 provides a similar example of a lead complex in the Beaufort Sea on 30 March 2000. In this figure, a combination of SSM/I and MODIS images is shown to illustrate the range of scales analyzed using such assemblages.
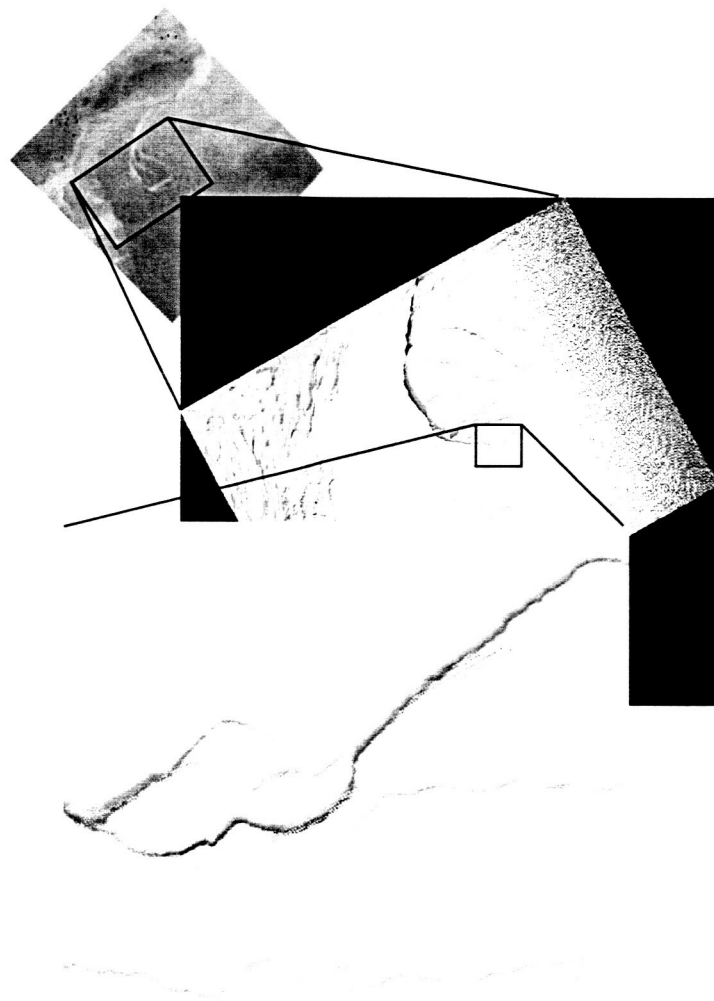
Figure 11. Lead complex and individual leads for 30 March 2000 in the Beaufort Sea as depicted in SSM/I 85 GHz brightness temperatures (top), MODIS channel 1 1-km data (middle), and MODIS channel 1 data at full resolution (250m) (bottom).

Based on such data sets, basic types of information can be retrieved relating larger-scale conditions to local conditions. These include relationships of lead formation with wind stresses (as indicated by speed and persistence of winds), relationships between these wind stresses and aggregate-scale ice drift, and characteristics of leads as they evolve in different ice regimes.

3.4 Sensitivity of Ice Lead Detection to Spatial Resolution

One of the goals of this project is to investigate the sensitivity to spatial scales of the contribution of ice leads towards the energy budget of the ice/lead surface. A preliminary approach to this problem is to determine how the spatial resolution of the imagery effects the detection and classification of the leads. The 50m resolution raw SAR radar backscatter imagery was resampled to the pathfinder grid at resolutions of 250, 500 and 1250m in the Beaufort Sea region. Examples of the 250m 500m and 1250m images used for this task were shown earlier in Figure 11. Two different thresholds were used to classify the SAR imagery into lead/no lead classes. Table 1 shows the percentage of ice lead as a function of resolution for the two different threshold choices. The results suggest that the percentage of lead pixels may not be very sensitive to spatial resolution, at least in the case when thresholds are used to classify the leads. This is somewhat surprising, and differs with most previous studies. Those studies, however, focused mainly on changes in estimated lead fraction as a function of resolutions finer than those used here. More research will be done exploring this sensitivity with more sophisticated classification schemes such as a maximum likelihood classifier noted in the next section. If these results hold, they would indicate that using finer resolution MODIS imagery (250m and 500m) does not offer gains in accuracy versus 1-km MODIS and 1.25-km AVHRR resolutions. The results also suggest that, for basic lead/no-lead mapping using thresholding, MODIS may not offer significant gains versus AVHRR. More work is needed to determine whether this is typical for other cases, since one would expect that the better radiometric accuracy and/or finer spectral resolution of MODIS should translate into differences in mapped lead fraction between MODIS and AVHRR. Future research will also investigate the effect of resolution on ice lead orientations.

Table 1 Percentage lead pixels for three resolutions and two thresholds

Resolution	Low Threshold	High Threshold	Percentage lead pixels (%)
250 m	0	25	14.55
500 m	0	25	14.60
1250m	0	25	14.80
250m	0	35	42.61
500m	0	35	42.69
1250m	0	35	42.70

3.5 Lead Mapping and Statistics from Multisensor Data

Retrieval of lead statistics was carried out using manual interpretation as well as with an automated, object oriented approach. The latter is based on the LEADSTATS routines developed by Dr. Jeffrey Key, and which has been applied by us previously to AVHRR and Landsat data. LEADSTATS requires as input a binary image consisting of "probable non-lead" and "probable lead pixels". The routines use spatial tests to group pixels into lead segments, and segments into likely continuous leads. Length, width, area, and orientation are then calculated for each lead and lead segment. This information can then be combined with lead surface conditions (estimated using the data fusion methods noted above) and ice pack characteristics (from RGPS, for example) to characterize the basic lead properties that are significant in turbulent flux calculations.

Among the data sets that we have acquired or are assembling include a sequence of 16 RADARSAT images collected for the Barrow area during Aerosonde UAV flights in April-May 2002, and a sequence of 12 SAR images spanning freeze-up through late spring for the Barrow area for October - April 2002. We expect to be able to find at least a few occurrences of near-coincident clear-sky MODIS and AVHRR images corresponding to these SAR data.

We also analyzed aircraft passive microwave imagery acquired during the SHEBA experiment. An example from one of these flights is shown in Figure 12. This image is a mosaic of AIMR tracks from several NCAR C-130 overpasses, and shows the result of the application of channel combinations for lead mapping. An advantage of these data is their spatial resolution (approximately 100m), availability of other SHEBA data including coincident high-resolution video and skin temperatures from the C-130, and availability of, for this particular case, a 50-m resolution MODIS Simulator image acquired by the NASA ER-2. Our intent was to use these data to investigate translations across scale. In particular, one of the leads within this image was studied extensively in the field, and served as a test case for the flux calculation experiments.
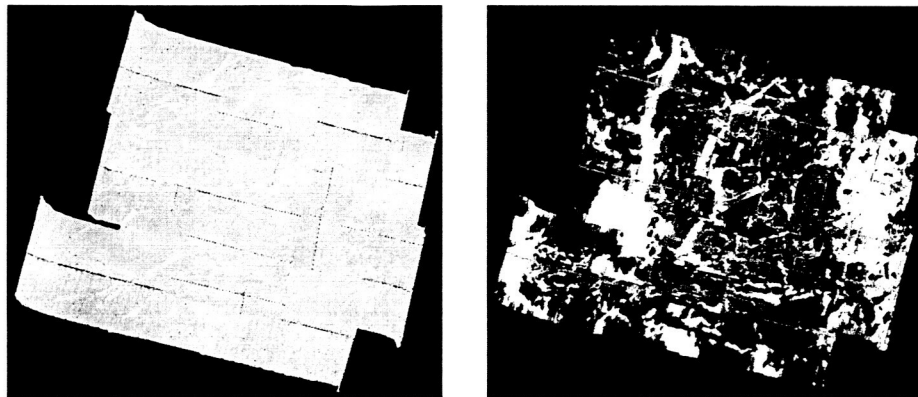

Figure 12. 90 GHz vs. 37 GHz spectral gradient (left) and ice type classification (right) using NCAR C-130 AIMR passive microwave data acquired on 20 May 1998 during the SHEBA experiment.

Output from the LEADSTATS lead object mapping is illustrated in Figure 13. In this case, a RADARSAT image acquired on 3 October 1998 was processed to extract lead statistics. The routine successfully identified the largest leads and provided realistic lead widths, lengths and orientations.
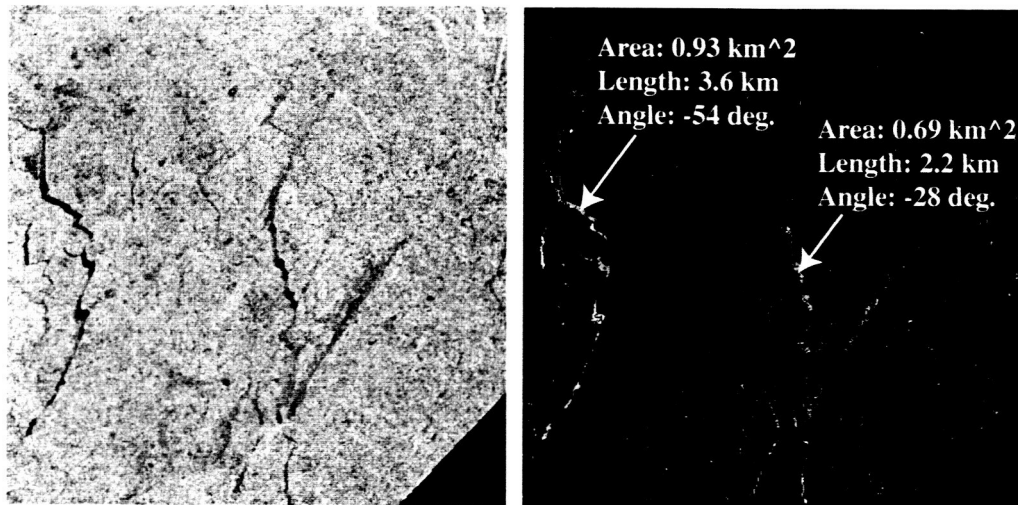

Figure 13. Application of the LEADSTATS lead statistics procedure to a RADARSAT image (left) acquired on 3 October 1998. The LEADSTATS output (right) shows areas considered likely to be leads in red and possible leads in yellow. Also shown are the LEADSTATS-derived statistics for the two leads with the largest estimated areas.

Compared to visible- and thermal-band imagery though, leads in SAR data have a more ambiguous pattern, with older patches of smooth first-year ice having backscatter values similar to recently opened leads. The high backscatter characteristic of new leads when winds are relatively strong is also similar to that from ridges and some multiyear ice locations. Thus, simple thresholding to identify "probable leads" pixels, which works well for visible- and thermal-band imagery, is less effective for SAR data. Further work is needed to refine the processing to accommodate these differences.

The SHEBA data sets also provide the means for retrieving detailed lead statistics for individual days during the flight period of the NCAR C-130. The role of these data in our analysis was to provide estimates of lead conditions at fine resolutions not achievable from RADARSAT, AVHRR, or MODIS. These statistics estimated from fine-resolution data were then be compared to satellite-derived statistics to assess how well the statistics and analyses translate across scales from 1 meter to 10's of kilometers. Our analyses of these data included derivation and interpretation of lead width, lead orientation and total number of leads from AIMR imagery for portions of the flight coverages on 5 days in May. Of these days, 2 days have RADARSAT imagery acquired on the same day, while 2 additional days have SAR imagery available for subsequent days. Our intent was to compare the lead statistics acquired from the AIMR data with similar statistics estimated from SAR and, for one of the days, statistics from ER-2 MAS, NTM and AVHRR imagery. This coverage period also includes high-resolution video and skin temperature measurements from the C-130. This task was started but was not completed by the end of the project. We expect to follow up with this work in a future effort.

18

A time series of AVHRR and SSM/I data were examined to identify cases useful for investigating lead conditions on a local through basin-wide scale. We have focused on two periods - the period during the SHEBA experiment and the period following the launch of MODIS. Since the project depends on examining the effects of different lead development stages on heat fluxes and the use of multisensor imagery to map these stages, it was important to find cases where the evolution of leads could be examined from initial formation onward. Animations of AVHRR Polar Pathfinder albedo and skin temperature images were used to identify events that might fit these requirements. An interesting lead formation event that provided the necessary criteria was identified as occurring in the Beaufort Sea beginning on 7 March 2000. Active lead formation persisted for approximately 3 weeks, with new leads forming and older leads re-freezing. Once this case was identified, considerable effort was expended searching for, obtaining, and georeferencing a set of RADARSAT SAR, MODIS, and AVHRR imagery that was as nearly coincident in time and space, that provided a large expanse of clear sky coverage, and that included a range of lead conditions. The area covered by the co-registered SAR, MODIS and AVHRR imagery is shown in Figure 14, along with the boundary of the larger region being used to assess overall ice conditions associated with the lead complex.

The sub-region data set includes MODIS 250m, 500m and 1 km channels acquired on 20:40 UTC on 28 March, 2000. The RADARSAT SAR image (full-resolution ScanSAR) was acquired at 16:12 UTC on the same day, with AVHRR Polar Pathfinder data were collected at 17:00, also on the same day. Thus, the image times differ by less than 4 hours. This data set, along with the lower-resolution data we have assembled for the larger scale, is thus adequate for testing all elements of the project. However, more such cases would be helpful, and we are continuing to search for similar conjunctions of data and conditions. Figures 15a-15f depict examples of the SAR, MODIS and AVHRR imagery that make up the March case study data set. Note the extent of the lead complex, and the range of different lead conditions (width, skin temperature, backscatter) in these images.
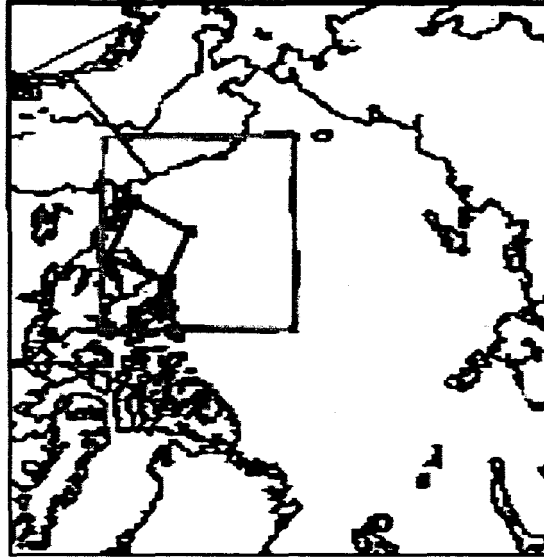
Figure 14. Area of coverage for the March 2000 lead case study. The SAR, MODIS and AVHRR coverage is indicated by the red box. The green box depicts the larger analysis area being examined with meteorological data, ice motion, and AVHRR and MODIS imagery.

Carrying out this georeferencing and merging of the March case data required the following tasks:

- Installation of ASF SAR processing software (data extraction and georefencing) to a CCAR linux computer.
- Construction of new software which interfaces with the SAR software to resample raw SAR imagery to a user specified pathfinder grid.
- Installation and implementation of MODIS processing software to allow resampling of MODIS swath imagery to a user specified pathfinder grid.
- Construction and implementation of software to resample Polar Pathfinder AVHRR data to a user specified pathfinder grid.
- Create SAR datasets on the same pathfinder grid for both 1250m, 500m and 250m resolutions.
- Apply software to create spatially coincident data sets on a 1250m resolution pathfinder grid for SAR, MODIS and AVHRR imagery.
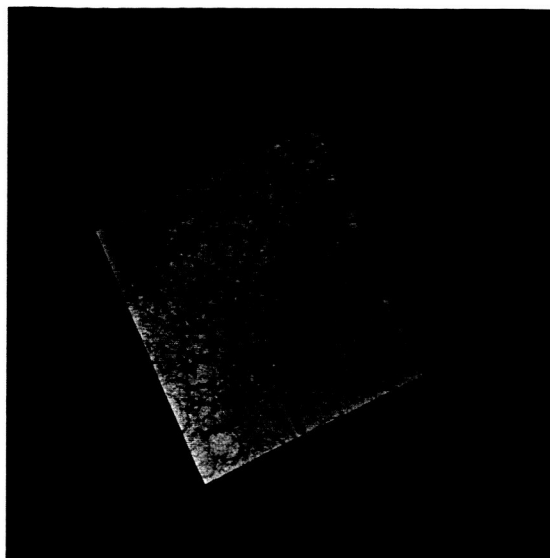
Figure 15a. RADARSAT ScanSAR baskscatter image at 500m resolution 3/28/00 16:12 UT for the merged-image sub-area.
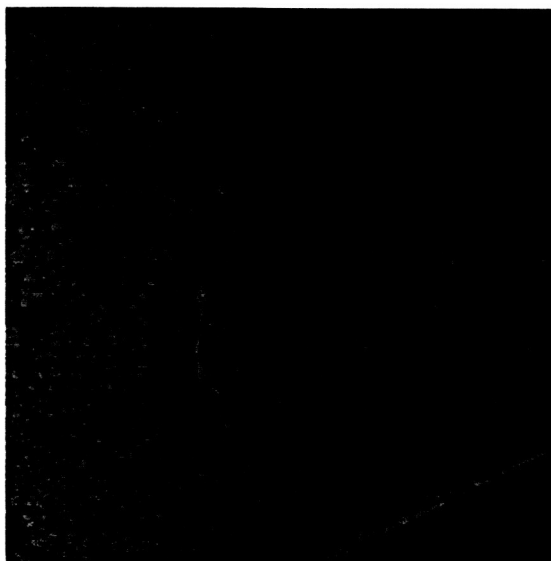
Figure 15b. 250-m resolution subset of the ScanSAR image in Figure 1a.

Figure 15c.   MODIS channel 31 (10.8-11.3 micrometers) at 1250m resolution. 3/28/00
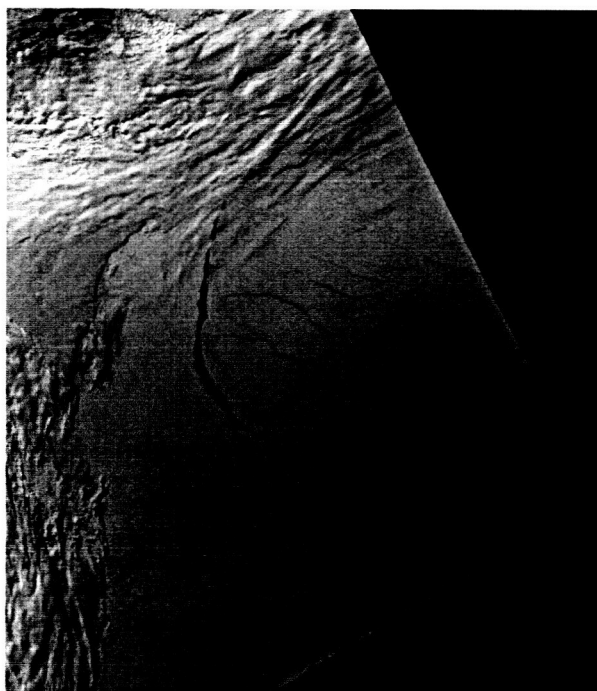20:40 UT

Figure 15d.   MODIS channel 2 1250m resolution the MODIS channel 2 (841-876
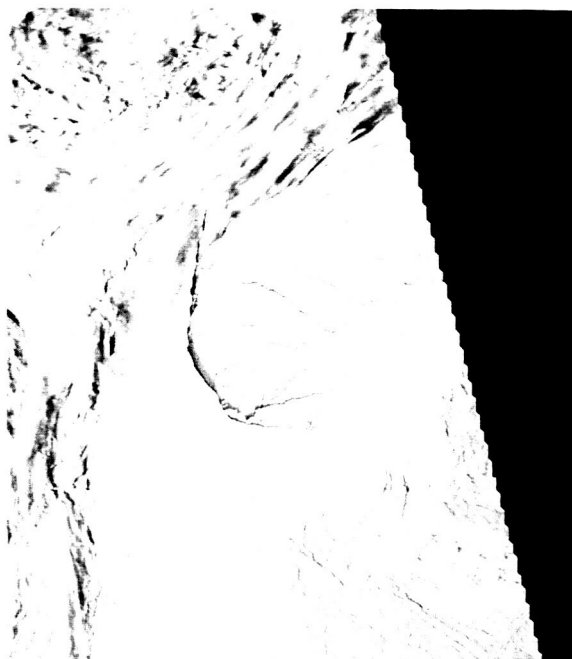nanometers), 3/28/00 20:40 UT

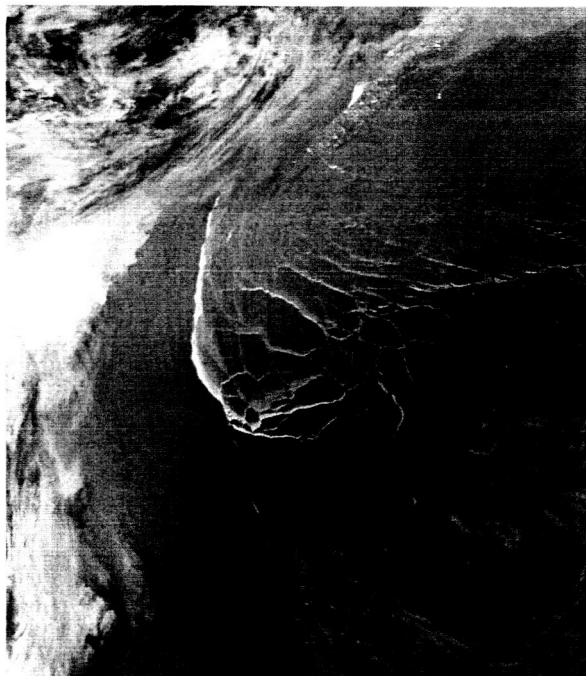Figure 15e. AVHRR Polar Pathfinder broadband albedo product 1250m resolution
3/28/00 17:02 UT

Figure 15f. AVHRR Polar Pathfinder skin temperature product 1250m resolution
3/28/00 17:02 UT

With this case-study data set in hand, we began the process of trying to relate local-scale lead conditions (time and rate of formation, orientation, width, and ice type) to larger-scale conditions. The analysis shows that the lead formation process for this case began in response to clockwise winds and ice motion associated with high pressure in the Beaufort Sea. Prior to 7 March, no leads were apparent in any of the image sets, but formation began quickly and progressed rapidly after 7 March. Of considerable aid in analyzing the time history of this lead event were animations of SSM/I 85 GHz brightness temperatures. In this case, the leads were large enough and brightness temperature contrasts were substantial enough to make the larger leads visible in the relatively low-resolution (12 km) SSM/I data (Figure 16).
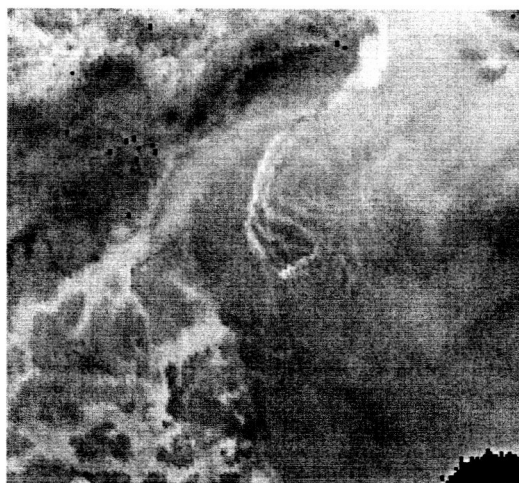

Figure 16. SSM/I 85 GHz brightness temperatures for 28 March 2000, showing the lead complex in the Beaufort Sea.

One of our findings from this portion of the research was the potential of AMSR-E passive microwave imagery for manual mapping of lead patterns and formation events. AMSR-E, with double the spatial resolution of SSM/I, improved radiometric performance and better geolocation, is capable of revealing individual leads within the 89 GHz channel data in particular. The 6km grid resolution at this frequency is nearly as fine as AVHRR GAC data which have been used in a number of investigations for lead mapping, but with the added advantage of much less attenuation by cloud cover. Using a case study of AMSR-E sequences, we investigated the patterns of formation and distribution of large leads in the western Arctic in conjunction with NCEP wind fields. Figure 17 shows examples of this analysis. We tested several digital means of identifying leads in these data, but given the time constraints in the project we decided to map leads manually. The leads in Figure 17 are indicated by the red and green lines, with red lines representing relatively newly-formed leads and green lines indicating older but still visible lead complexes. A particular advantage of lead mapping at this scale is that it provides a means of depicting changing lead conditions on daily intervals over large areas. This provides a contrast between more typical lead mapping done using higher resolution imagery such as RADARSAT. Applications of these data for examination of relationships between atmospheric and ice conditions and leads at different scales is discussed in Section 4.
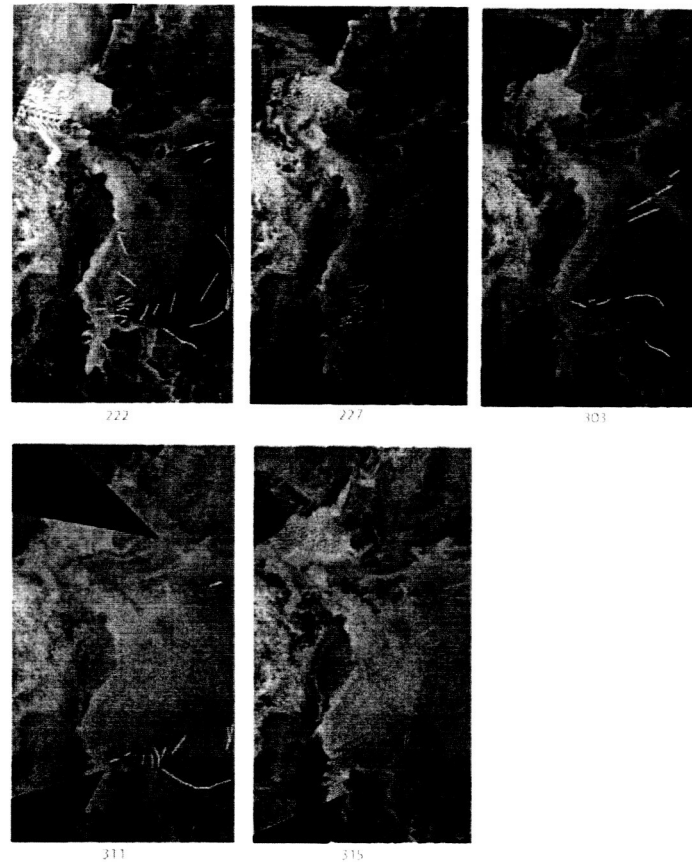
Figure 17. Manual mapping of leads using AMSR-E 89 GHz passive microwave images.

3.6 Data Fusion Methods

After a search for available fusion software, the MATLAB "FuseTool" library of 12 data fusion routines was installed and tested, as were routines available in the PCI Geomatica remote sensing package. The MATLAB toolkit provides a variety of sophisticated fusion methods, including fusion based on wavelets and neural networks. The PCI package includes the more common fusion routines such as hue, saturation, and intensity conversion and other methods designed primarily to combine lower-resolution multispectral information with higher resolution single-channel data. The multispectral sensors are typically the lower resolution of the co-registered image sets, so the intent is to add as much of the high-resolution detail as possible to the color or pseudo-color channels.

Figure 18 shows an example of the application to SAR and AVHRR data of a discrete wavelet transform fusion method available in MATLAB FuseTools. The data used are from the SHEBA January case study. In this case, each image type contains some duplicate information but also some unique aspects. The fusion method attempts to retain high-frequency variations as well as tone differences. The result is a single image that offers most of the information content of the separate backscatter and skin temperature images. We have experimented with the full set of FuseTool routines, and find that the

25

shift-invariant wavelet transform seems to do the best job at maximizing the lead information in the fused images.

One advantage of fusion is its ability to highlight cases where leads would be detected in one image type or the other, but not in both. For example, the smaller leads in the center of the image area in Figure 18 appear as warm ice but ice with high backscatter. These features would likely be classified as leads in the skin temperature data but not in the SAR image. Features with low backscatter typical of leads but with skin temperatures more in keeping with thick ice are also apparent. The fused image provides a means of discriminating these types of features which are probably relatively thick, smooth refrozen leads, from newer, thinner-ice leads. Since the heat flux will vary substantially between the two features, misclassification can be a significant problem. We subsequently used these merged data sets and resulting lead information to quantify the significance of the additional lead detail in terms of fluxes of such differences in image content (see Section 3.7.5)

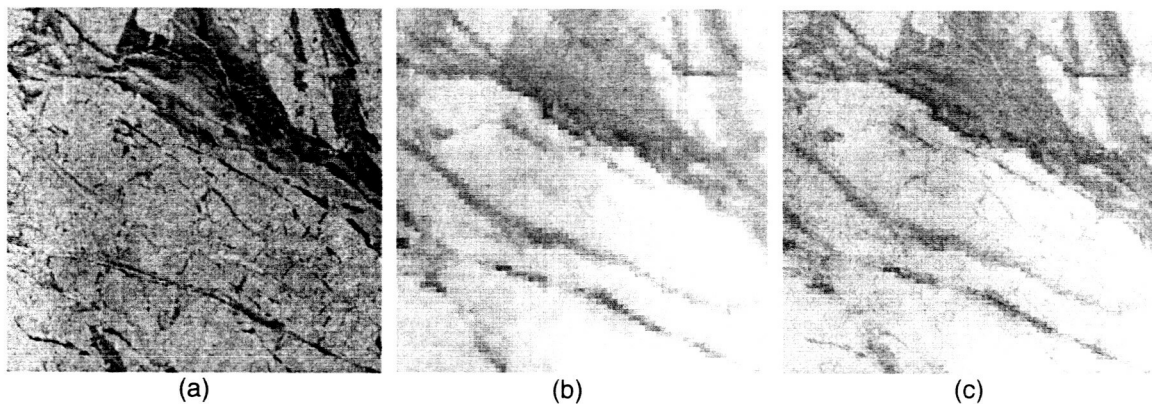(a)   (b)   (c)

Figure 18. An example of the fusion of RADARSAT SAR backscatter (a) with AVHRR skin temperatures (b) for a subsection of the SHEBA January case study area to yield a merged product (c) that combines information from both sensors. The image sections shown are 70-km by 70-km. Original spatial resolutions of the data for this case are 200-m (SAR) and 1.25-km (AVHRR). The AVHRR image gray tones are reversed such that warm features are darker.

Another, more traditional, approach for of data fusion is to combine the information content of multiple spectral channels via principal components or image classification. To date, we have tested maximum likelihood classifiers as a fusion tool. Of the three sensors, AVHRR and MODIS provide the most similar information, so it was decided to test the maximum likelihood approach using the two AVHRR products and the SAR imagery. Preliminary results suggested that 5 classes best describe the three images: cloud, no-lead ice1, no-lead ice2, lead ice 1 and lead ice2. The algorithm was thus trained with 3 channels (AVHRR albedo, AVHRR temperature and SAR radar backscatter) and 5 classes. Comparisons showed that the maximum likelihood classification captured more lead pixels while minimizing the number of falsely classified pixels. It is expected that further training would result in a substantial decrease in the quantity of false classifications.

Data visualization techniques provide another simple fusion method useful for interpreting information in different channels . Data combinations such as those in Figure 18 were used to explore how different image types portrayed the same ice condition. For example, Figure 19 combines AVHRR skin temperature and SAR backscatter, using vertical relief and color, to highlight areas where temperatures are high and backscatter is low, etc. In the lower panel, backscatter is on the z axis with temperature shown in color. It is apparent that there are low backscatter areas with low temperatures, which are likely areas for misclassification as leads, as discussed above for the narrow leads in the center of the images.
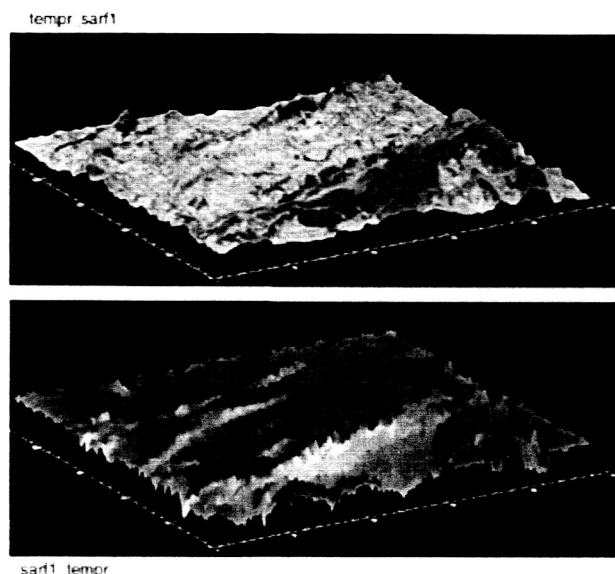
Figure 19. Merging, via shaded relief mapping, of skin temperature and SAR backscatter. (Top) temperature (z axis) and backscatter (color). (Bottom) backscatter (z axis) and temperature (color).

3.7 Investigations of Physical Characteristics, Lead vs. Forcing Relationships, and Parameterization Approaches

3.7.1 Barrow-Vicinity Case Studies Using Aerosondes, RADARSAT, AVHRR, and MODIS

A new capability available for this project is the availability of Aerosonde UAV products. The Aerosondes our group is operating from Barrow as part of the NSF Long-term Observations and Modeling effort carries a digital camera, a KT-11 profiling thermometer (with plans for a lidar system) and a video system with a real-time transmission range of over 60km. During NSF-sponsored field campaigns underway March and April 2001, 2002 and 2003, we coordinated Aerosonde flights with RADARSAT, AVHRR and Terra and Aqua overpasses to acquire near-coincident data sets. In these cases, the Aerosonde serves as a research aircraft providing detailed views of lead conditions that can then be compared with the lower-resolution SAR and other image types. Figure 20 shows an example of an approximately 50-m wide lead.

Transects of such photographs, along with skin temperature retrievals, were obtained for a complex of near-shore leads. For this case, 20 RADARSAT scenes were obtained for the period from 7 - 17 April. Figure 21 shows Aerosonde-measured skin temperatures during passes across this lead. We prepared several of these cases for use as validation of our flux modeling experiments.
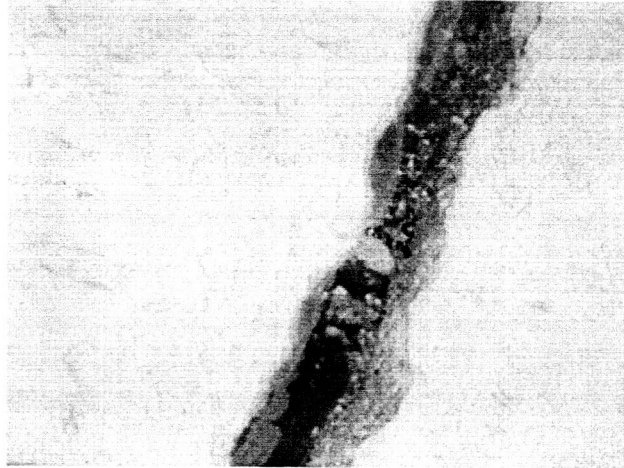

Figure 20. An example of low-altitude aerial photography of lead conditions off-shore of Barrow, Alaska on 15 April 2001. Photographs were obtained using the Aerosonde UAV to complement SAR, AVHRR, and MODIS imagery collected during the same period.
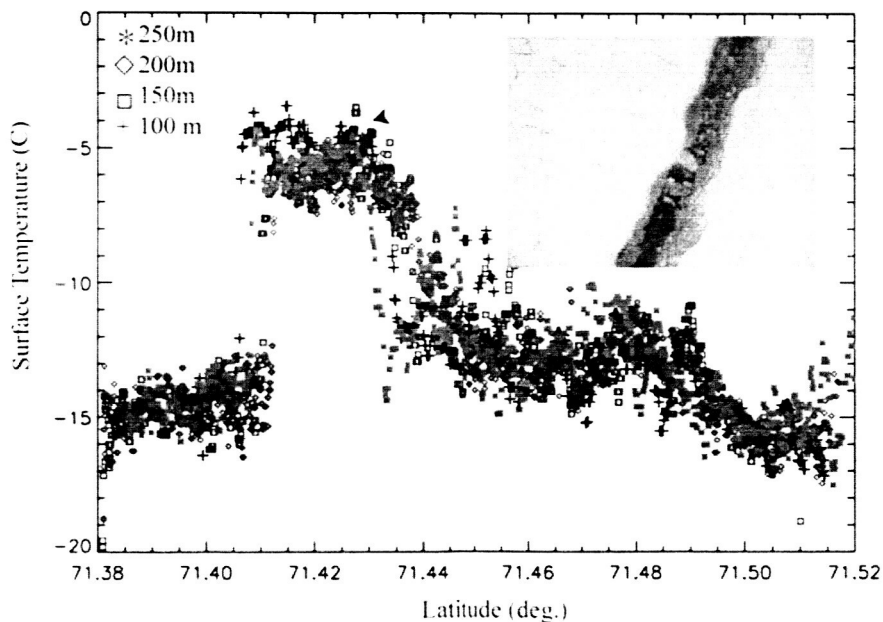

Figure 21. Transects of skin temperatures acquired at different flight altitudes over an off-shore lead (inset) north of Point Barrow in April 2001. Thick shore-fast ice is present to the south of the lead, with the lead evident by the rise in skin temperature at approximately 71.42 degrees N latitude. Temperatures north of the lead indicate new and young ice as well as possible heating from the adjacent lead.

The ability of the UAVs to acquire high-resolution sequential aerial photographs in conjunction with skin temperatures and atmospheric conditions (air temperature, relative humidity and wind speed and direction) provides the means to investigate model assumptions regarding parameterizations such as the prescription of leads as congelation vs. frazil leads (i.e., completely frozen-over leads vs. leads with some open water) solely as a function of specified lead width (in the Alam models, leads wider than 20 meters are assumed to be frazil ice leads). The data allow us to examine lead ice conditions in conjunction with lead width as well as wind speed and direction. Wind speed and direction (fetch) is known to affect frazil vs. congelation freezing, but no data sets have previously been available to investigate these relationships. Figure 22 illustrates a case where we examined skin temperatures and air temperatures directly upwind and downwind of different types of leads (seen in the mosaic of Aerosonde photographs). Location A consists of an area with a large frazil-ice lead, while Locations B and C are narrower leads that appear to be covered by congelation ice. In this case, we see an apparently significant contribution to warming of the boundary layer by the large frazil lead, whereas no discernable effect is measured downwind of the smaller leads. This is consistent with observations and model assumptions regarding heat output from open vs. refrozen leads, as well as the importance of lead width on producing heat and moisture plumes sufficiently large to penetrate above the near-surface level.
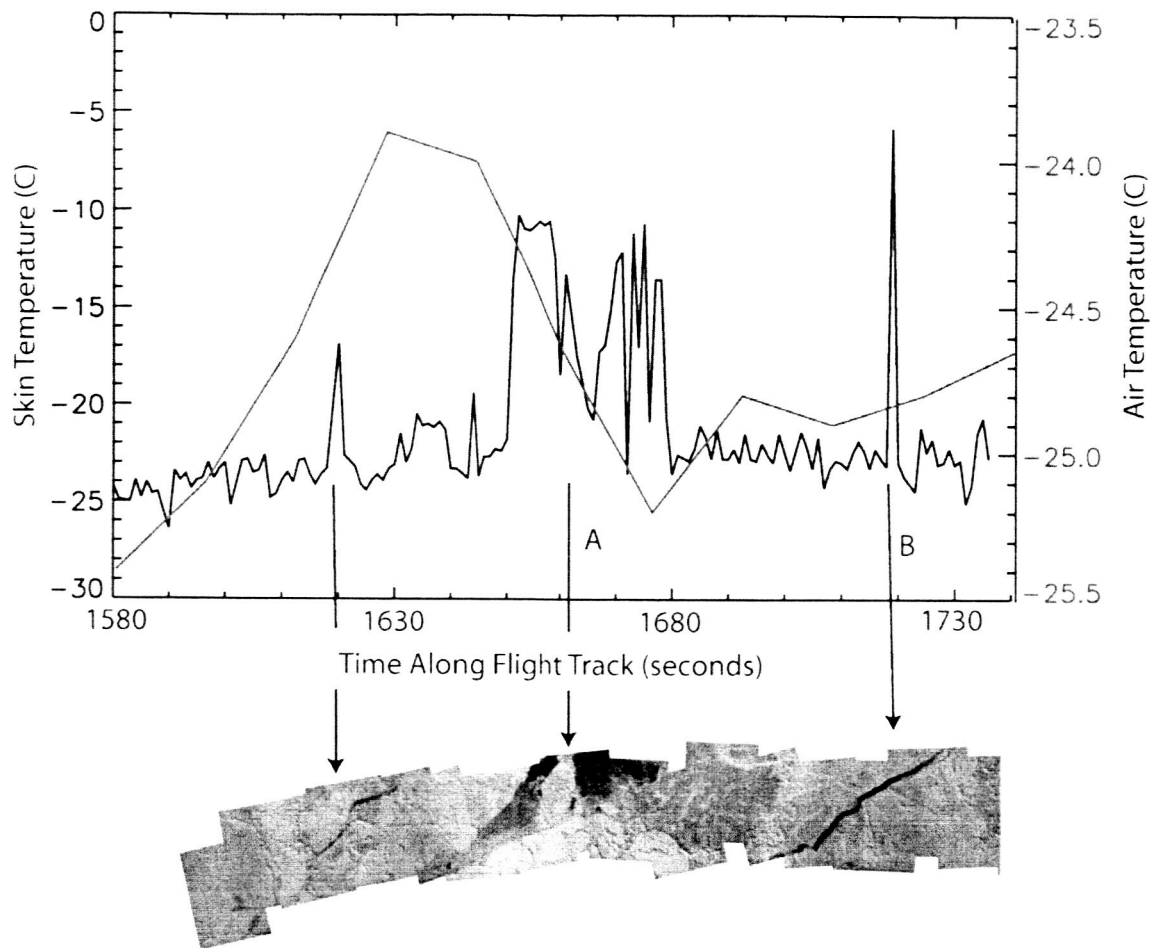
Figure 22. Effects of different types of leads on the atmospheric boundary layer, as observed using Aerosonde aerial photographs and air and skin temperatures obtained from a flight altitude of 200m. Skin temperatures and air temperatures are shown in the green and black lines respectively. The spikes in skin temperature associated with the warmer leads are readily apparent. The downwind effect of the large lead at Location A amounts to a 1 degree increase in air temperature. Given the relatively high flight altitude, a 1 degree increase in air temperature implies significant heat input into the near-surface boundary layer.

3.7.2 Analysis of Lead Formation Processes

The sequences of SSM/I images were analyzed in comparison to co-registered NCEP sea level pressure (SLP) fields and Polar Pathfinder sea ice motion data consisting of blended SSM/I, AVHRR, and buoy vectors. The SLP fields for 5-8 March cover the period when no leads were visible, through initial formation of the large leads (Figure 23). The response of the ice pack to this synoptic situation is shown in the ice motion data in Figure 24. In this case, pre-existing leads may have been present, refrozen to sufficient thickness and with snow cover deep enough to render them invisible in the AVHRR,

MODIS and SSM/I data (we have not yet acquired a SAR image for this "pre-lead" time). Networks of leads are known to form and re-freeze in this area, yielding a characteristic "diamond" pattern that has been linked to a combination of prevailing wind stress and ice properties.

The SLP data suggest stress buildup in the ice pack prior to 7 March, but the wind direction inferred from the SLP patterns are not entirely consistent with the general assumption that leads tend to form perpendicular to the wind direction. Examination of the ice motion fields (Figure 24) however, clearly show a pattern of ice drift that corresponds well to the location and direction of the lead opening. The motions indicate strong divergence in the area where the large leads have formed. The curvature in the motion field in the southern Beaufort Sea is also consistent with the direction and likely shearing motion of the southward portion of the lead complex.

This analysis could be extended further to derive statistics relating ice motion to lead patterns (rate of formation, width, and orientation), which serve as the basis for a general parameterization.
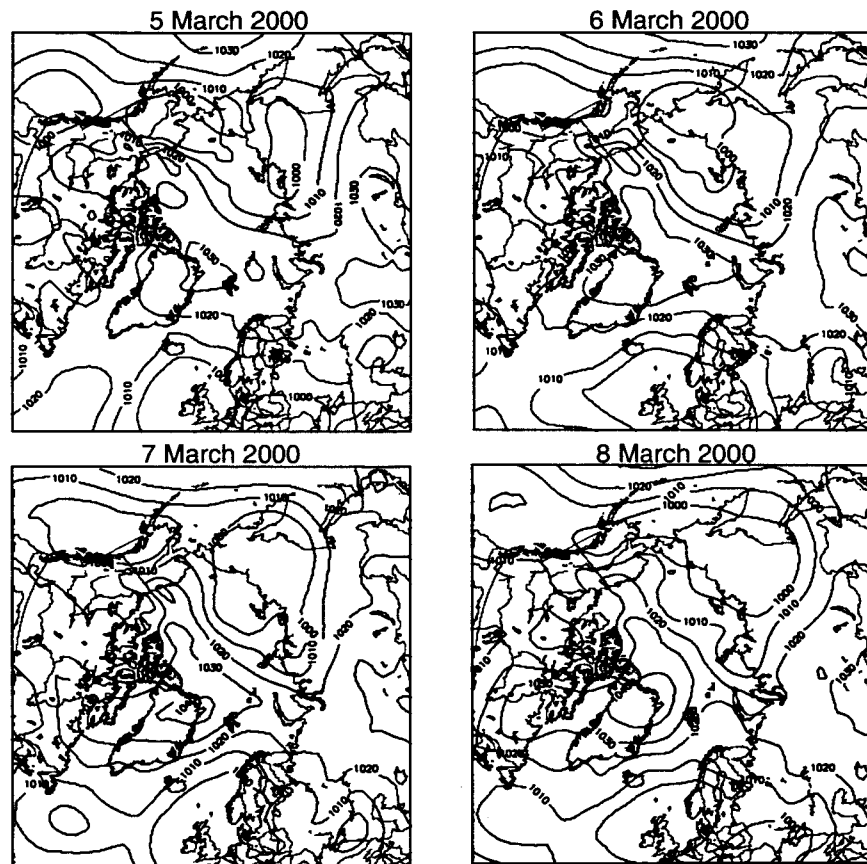

Figure 23. Sequence of NCEP sea level pressure patterns prior to and during the March lead opening event.
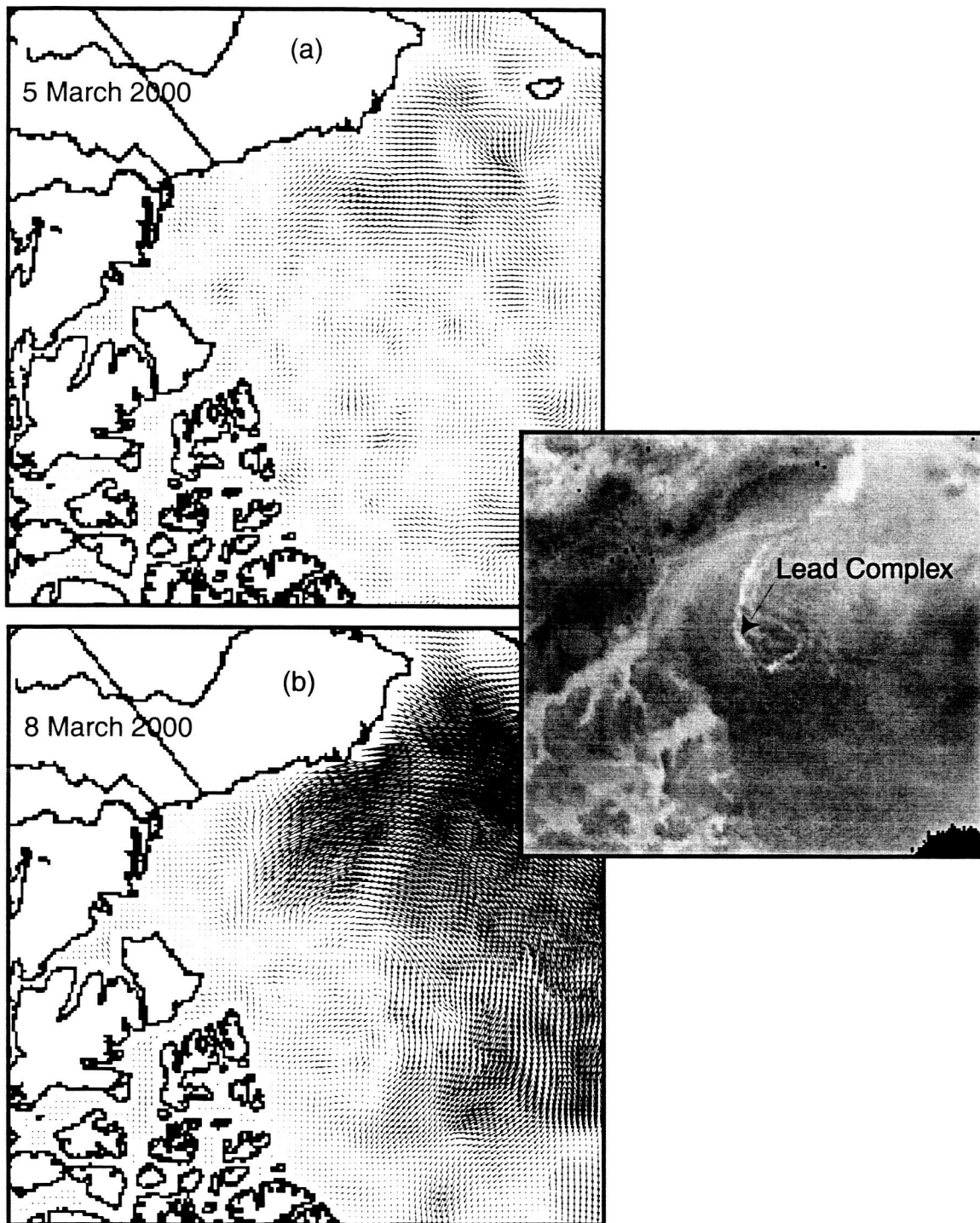
31

Figure 24. Polar Pathfinder ice motion data (a and b) and SSM/I 85 GHz image (inset). The SSM/I area corresponds to the area shown in the SLP maps. Note the apparent relationship between the lead location and orientation with the ice drift direction and location of maximum divergence.

A second lead case study was for 14-20 January 1998, located in the SHEBA field experiment area. This case had been selected earlier by SHEBA Phase 3 investigators as one of several cases upon which SHEBA researchers are focusing. For this time period, AVHRR Polar Pathfinder products were available, as were RGPS products and RADARSAT ScanSAR images processed by Harry Stern for the SHEBA project. Figures 25 and 26 show the time series of twice-daily AVHRR skin temperatures and SAR images. The effects of ice dynamics are apparent in the formation of new leads and slight rotation of the area.
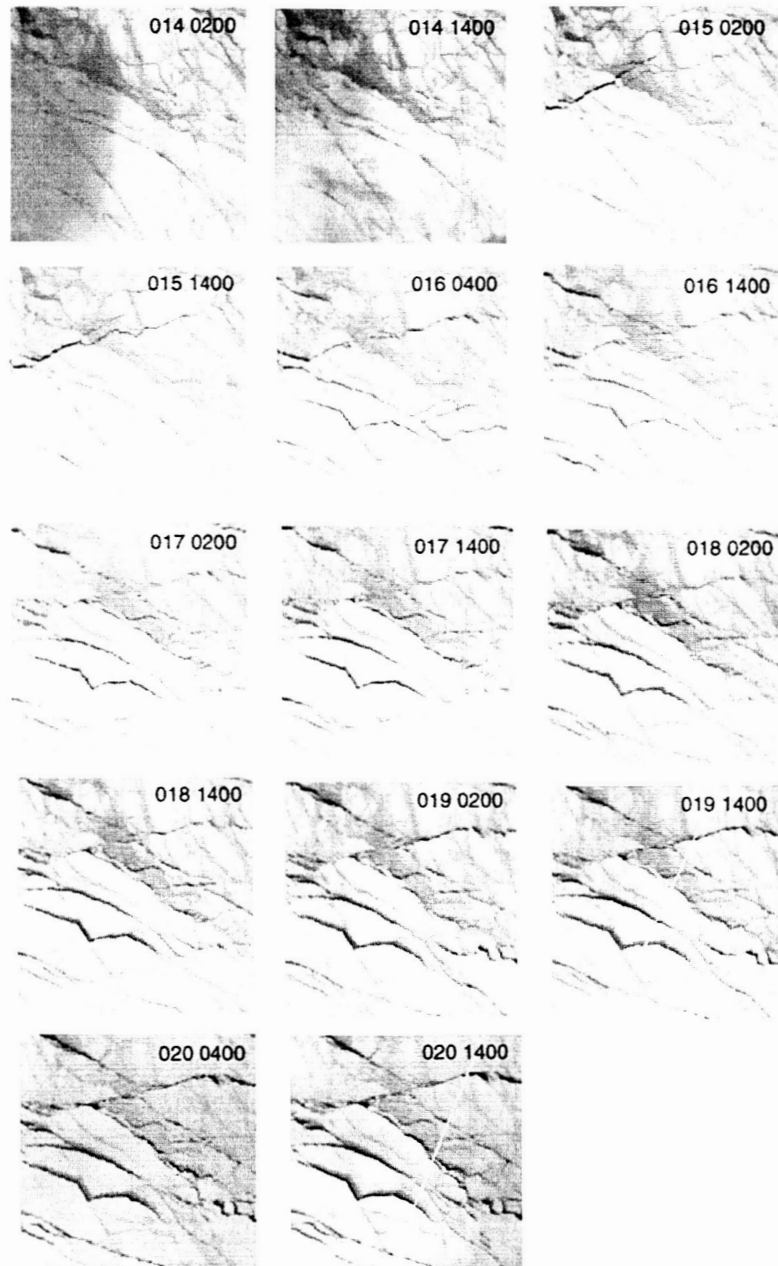

Figure 25. AVHRR skin temperature sequence for the 14-20 January 1998 (SHEBA) case study.
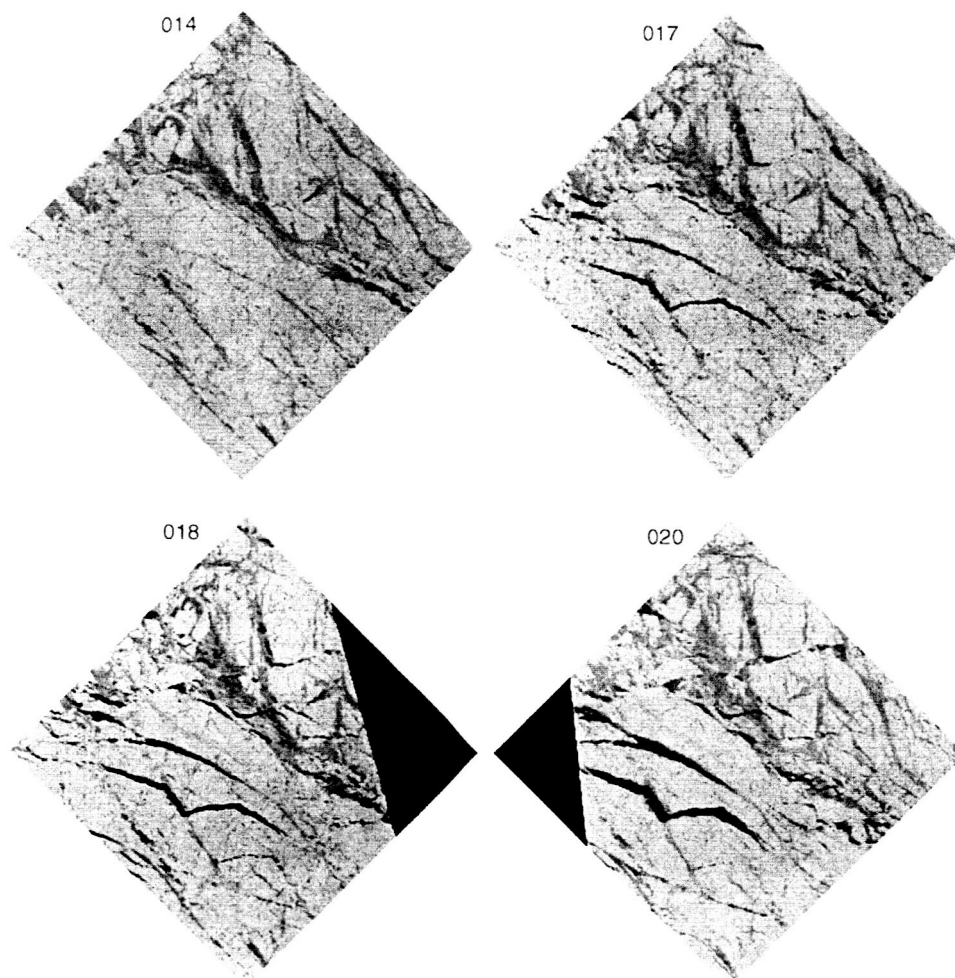
Figure 26. ScanSAR images for the 4 days of SAR data available for the January SHEBA case study. (SAR data courtesy RADARSAT International and Harry Stern [APL]).

3.7.3 Analytical Determination of Lead Characteristics and Scale Relationships using Ice Motion Data

During the 3rd. year of the project, we embarked on a new direction of research that would potentially allow us to directly estimate the characteristics of leads that develop under different ice drift conditions and at different scales. The thrust of this work was to develop, or at least set the stage for developing, means of parameterizing the lead characteristics resulting from this discrete movement using input from models capable only of providing the smoother, lower-resolution scales of data. We therefore use the ice motions at different scales to try to develop these relationships. The examples here illustrate our efforts toward this goal using analytical "lead generation" approach. As noted earlier, rather than requiring the assembly and merging of remotely-sensed images at different scales and then mapping leads at each scale, we instead use the approach of extracting ice motion at each scale and then deriving lead patterns from the motion fields.

34

A major impetus for this redirection was the realization that while our focus in Years 1 and 2 on assembly and analysis of multi-scale case studies spanning a range of ice and atmospheric conditions was yielding useful and interesting results, we were not going to be able to locate and examine enough case studies to yield basic insights into the relationships between large-scale conditions simulated by standard sea ice and climate models and the details of lead conditions (width, ice type, orientation) needed to incorporate our improved lead models into existing regional and global models. In addition to the level of effort needed to prepare the case studies, the occasions when there are coincident microwave, visible and thermal band imagery needed to identify detailed ice characteristics are relatively rare and limited in scope and spatial coverage. With this in mind, we developed a method that would make use of ice motion calculated at fine scales from RADARSAT data in combination with coarser-scale ice motions estimated from AMSR-E data to (a) artificially generate leads based on ice divergence and shear, (b) use these different scales to investigate ways of prescribing details of lead conditions from the kinds of information generated by large-scale models (i.e., large-scale ice motion, ice concentration, ice age and ice thickness), and (c) allow us to generate enough cases for useful comparisons to NCEP fields and remotely-sensed and estimated sea ice conditions.

Figure 27 shows two examples of lead formation. The situation depicted on the left would be typical of pure divergence. It represents the idealized view of an entirely open lead, with open water produced within a model grid cell only when there is positive divergence. The stair-step nature of the lead shown here is typical of actual leads. The situation on the right is one where motion is not divergent but instead is pure shear. Given the stair-step fracture pattern common within the ice pack, one can see that some open water is formed in sections of the lead, some (sub resolution in this case) open water patches will be present in the shear zones (the white areas), and the surface roughness within the grid cell.
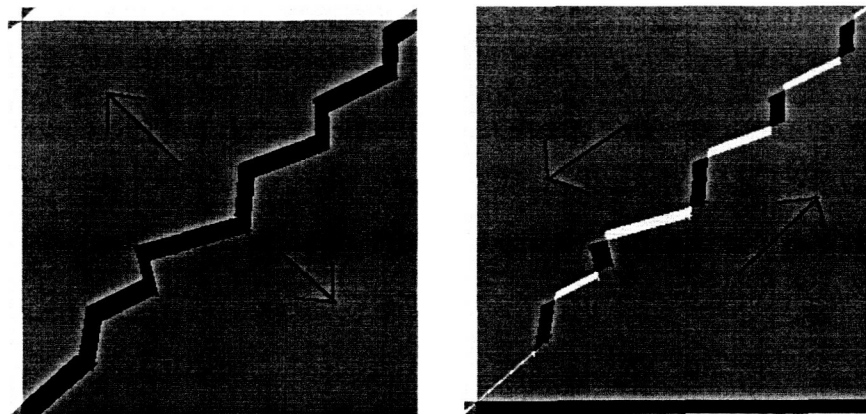

Figure 27. Illustration of lead formation under pure divergence and under pure shear.

To illustrate our approach, Figure 28 shows on the left, the baseline AMSR-E data used to generate large-scale ice motions (center) from sequential satellite images. The panel on the right depicts NCEP wind fields for this day. Figure 29 shows ice motions

calculated from sequential RADARSAT images for a fixed study area in the central Beaufort Sea (also indicated in Figure 29).
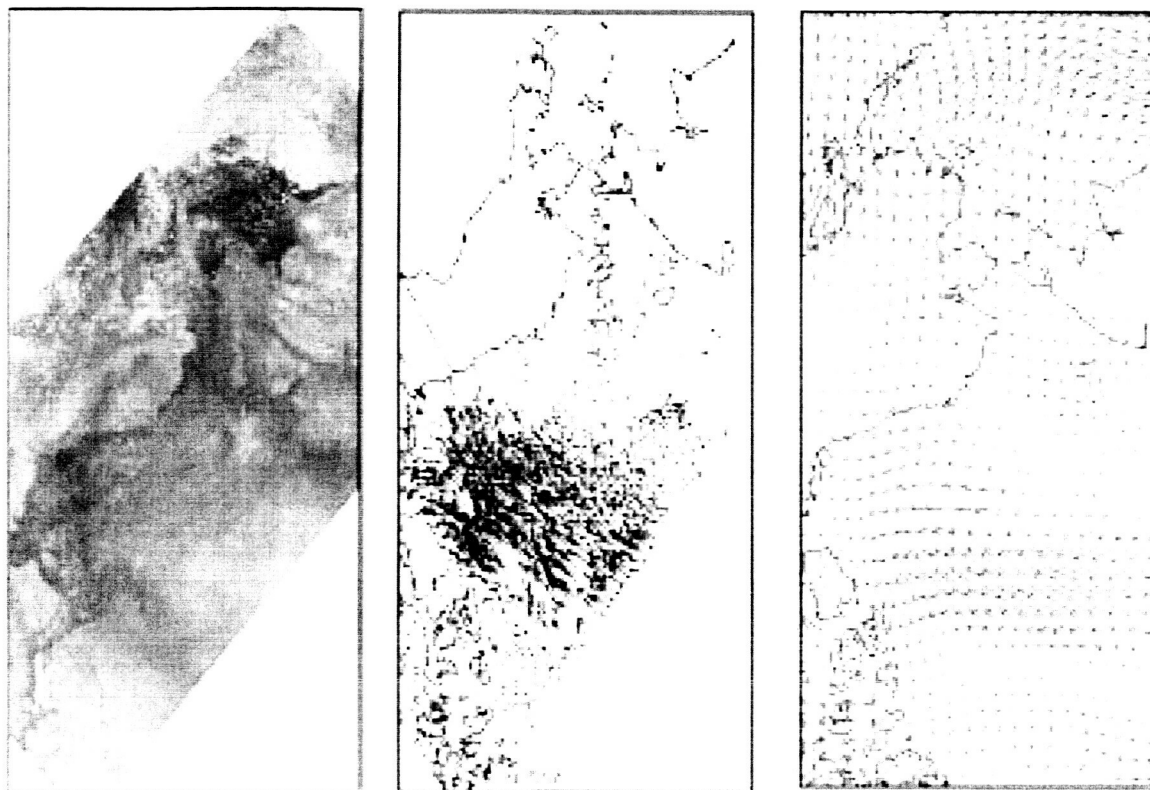

Figure 28. AMSR-E 89 GHz AMSR-E image (left), ice motions calculated from the AMSR-E images (center) and wind vectors from gridded NCEP reanalysis data (right).
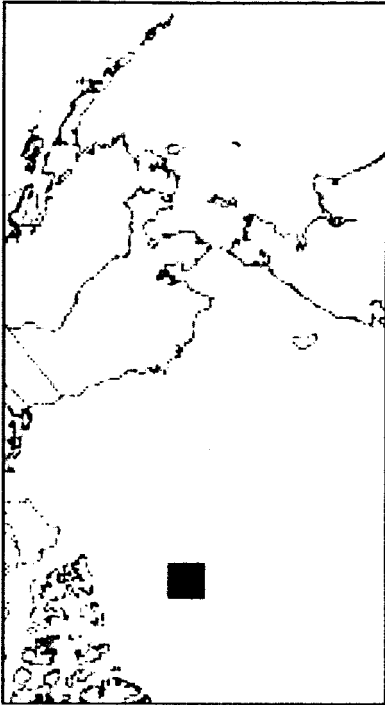
Figure 29. Study area used for SAR motion generation and comparison. The center of the nearly coincident velocity fields generated for this date are shown as dots. The area of coverage used was 200 km by 200 km centered at approximately 78 N and 156 W. The square is a representation of the coverage area but would be centered on each of the dots.

For this analysis, we selected an area north of Barrow for which we had obtained imagery for the same area for almost 40 consecutive days except for March 8 the period from Feb. 27 through April 7, 2003. The following presents several illustrative cases from this image set. Note that this sequence of cases covers a period of less than a month and a half, yet the variability in ice motion is very large. These show, in particular, some of the extreme ice-motion events. Four plots for each case. First is the NCEP surface wind field. Second is the ice motion from the AMSR 6 km data. This also shows the spotty nature of deriving motions from the passive microwave, but reveals that motion retrieval from AMSR-E is much better than vectors derived from SSM/I or from visible and thermal imagery, the latter of which are often obscured by clouds. The third plot presents vectors from calculated from the 200 meter RADARSAT ScanSAR data. The 4th plot is the divergence plots from the SAR vectors. In the AMSR vector map, the area covered by the SAR is shaded. In the SAR vector maps, the mean ice motion has been subtracted from each vector, so what is presented is the relative ice motion within the 200 km square area, which is the motion that produces leads within the 200km region.

For the first case, 6-7 March 2003, the large-scale ice motion represented by the AMSR-derived vectors (Figure 30, top left) differs markedly from the wind fields (top right). Such disagreements are rare in these and other situations that we have examined in previous studies. The differences here probably due to differences in time periods covered by the winds and the time span used for the pair of images used to generate the

ice velocities as well as errors in the NCEP wind fields. The large-scale ice motion shows a region of rapid ice movement in the central and eastern Beaufort Sea, with other regions showing relatively slow movement. The SAR motions in Figure 30 (bottom left) reveal the details of the motion patterns within the 200km region, and yield the shear and divergent motions that are the drivers for lead formation. Here and in most of our other cases, the ice can be seen to move as large plates, with lead activity concentrated at the plate boundaries. A key point to take from the vectors at these different scales is the degree to which increasing spatial resolution reveals the increasing degree to which the ice pack can be seen to move as a collection of discrete features (plates and at finer scales, individual floes). From the SAR motions, we then calculate the information shown in the bottom right panel of Figure 30, which represents the actual formation of leads and shear zones given the observed SAR motion. Note the correspondence between shear motion and divergence in the SAR motions with the lead production in the generated lead image in the bottom right.
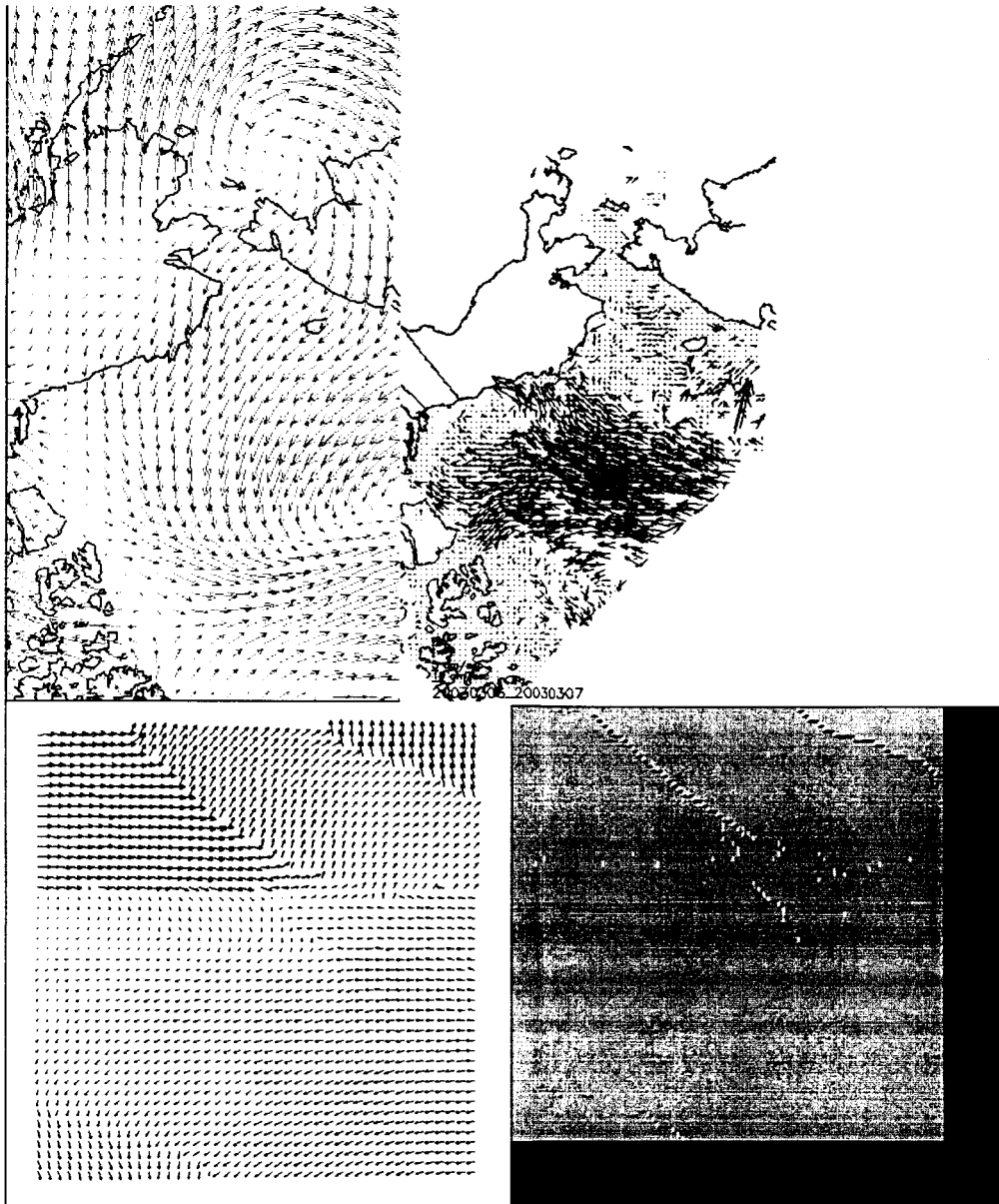
Figure 30. Multiscale analysis of winds and ice motion at different scales for 6-7 March 2003. NCEP winds (upper left), AMSR derived ice motions (upper right), RADARSAT-derived ice motions (lower left) and resulting "synthetic leads" (lower right).

Figure 31 shows the same analytical procedure for a case with extreme shearing. In this case, the NCEP winds imply rapid ice movement over a broad area of the western Arctic. In the AMSR motions, we see that this zone of rapid ice drift is more distinct and restricted to a specific area. In the SAR motions (recall that the residual motion is shown here, which is the motion that remains when mean motion within the box is subtracted from each vector. The residual motions reveal that within the region of rapid ice drift depicted by AMSR, individual ice plates move at different speeds relative to each other. The synthetic lead image shows the resulting pattern of leads generated by this shear.
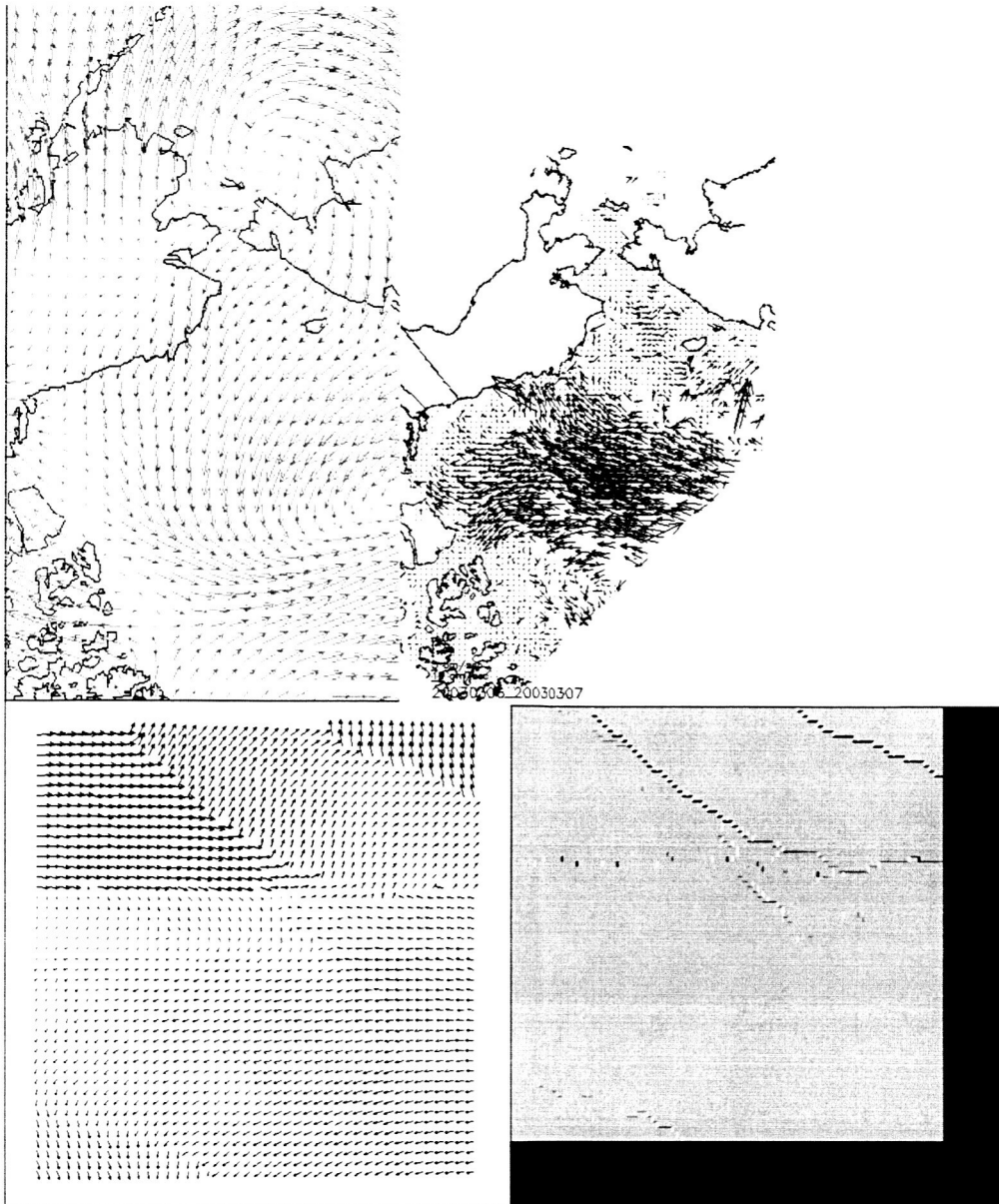
Figure 30. Multiscale analysis of winds and ice motion at different scales for 6-7 March 2003. NCEP winds (upper left), AMSR derived ice motions (upper right), RADARSAT-derived ice motions (lower left) and resulting "synthetic leads" (lower right).

Figure 31 shows the same analytical procedure for a case with extreme shearing. In this case, the NCEP winds imply rapid ice movement over a broad area of the western Arctic. In the AMSR motions, we see that this zone of rapid ice drift is more distinct and restricted to a specific area. In the SAR motions (recall that the residual motion is shown here, which is the motion that remains when mean motion within the box is subtracted from each vector. The residual motions reveal that within the region of rapid ice drift depicted by AMSR, individual ice plates move at different speeds relative to each other. The synthetic lead image shows the resulting pattern of leads generated by this shear.

39

The next three cases (Figures 32-34) demonstrate additional situations where shear-induced leads are generated during situations that would yield no open water production using coarser-scale modeled or observed ice motions. In Figure 32, the NCEP winds and AMSR motions both show a large-scale rotation pattern in the northern Beaufort Sea. When one examines the SAR motions and the resulting calculated lead production, we see that this rotation also appears at this much finer scale, with shear leads produced along the edges of the rotating plates. Figures 33 and 34 show cases where the coarser-scale data suggest general convergence of the ice pack. At the SAR scale though, we find that even in net convergent zones, relative motion between adjacent plates yields areas of shear that do not appear as coherent leads at this scale, but nevertheless represent areas where small areas of open water might form.
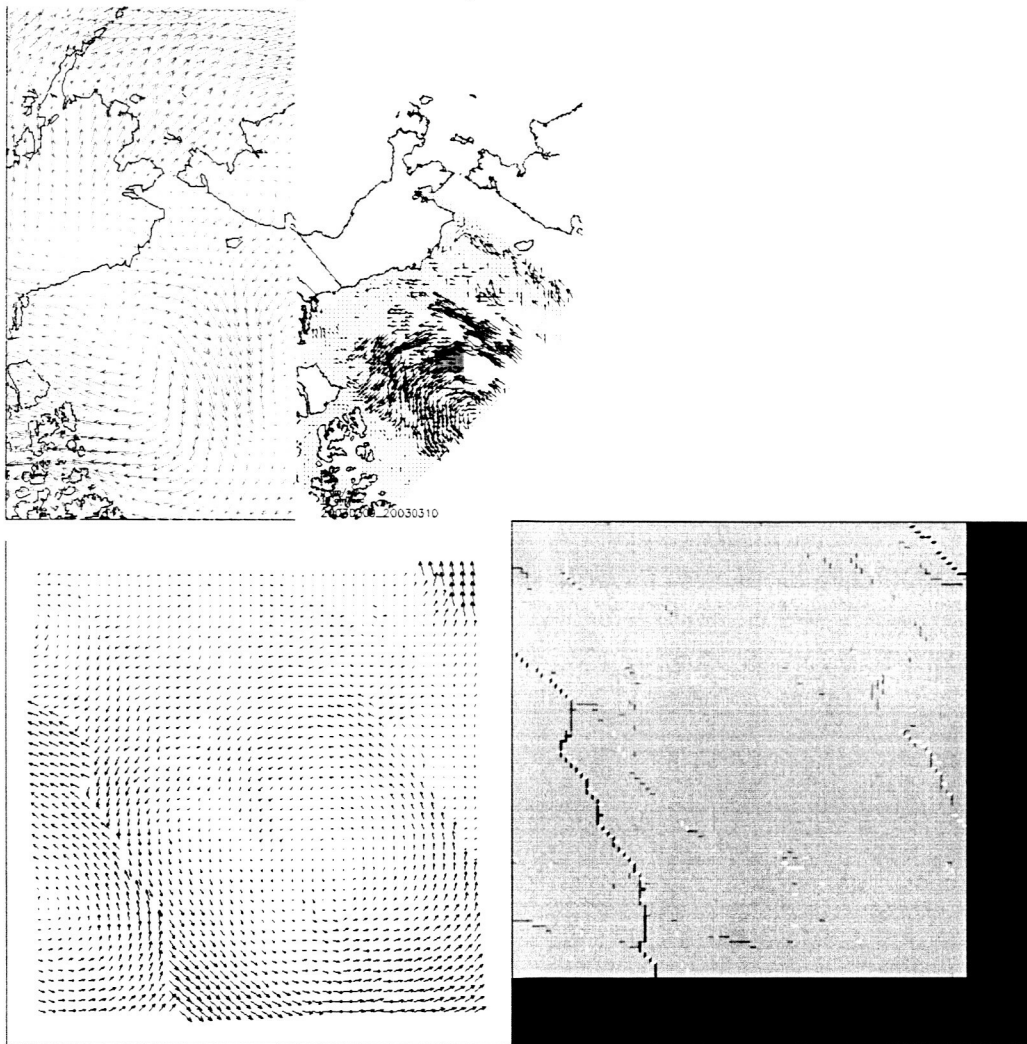

Figure 32. A case (9-10 March 2003) with rotational motion seen at each scale, yielding some open water production along the edges of rotating plates.
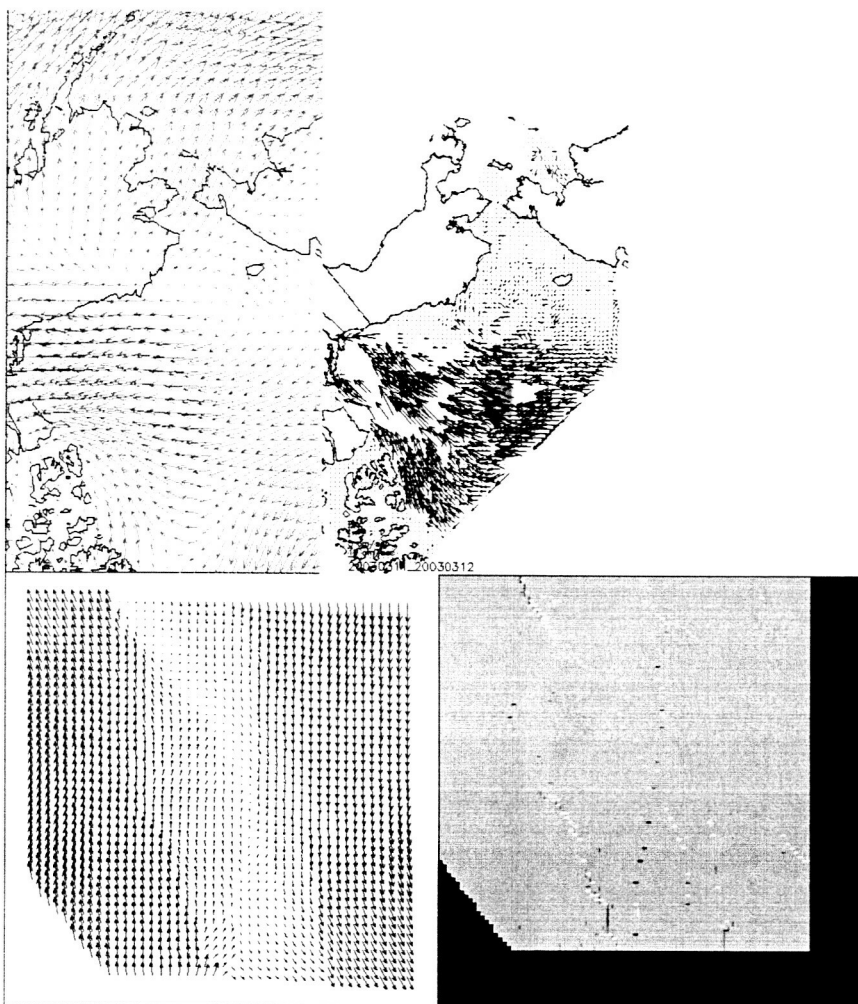
Figure 33. Motion and synthetic leads for 10-11 March 2003. Even in a situation that appears convergent in the small-scale motions, some open water production is present in the synthetic leads.
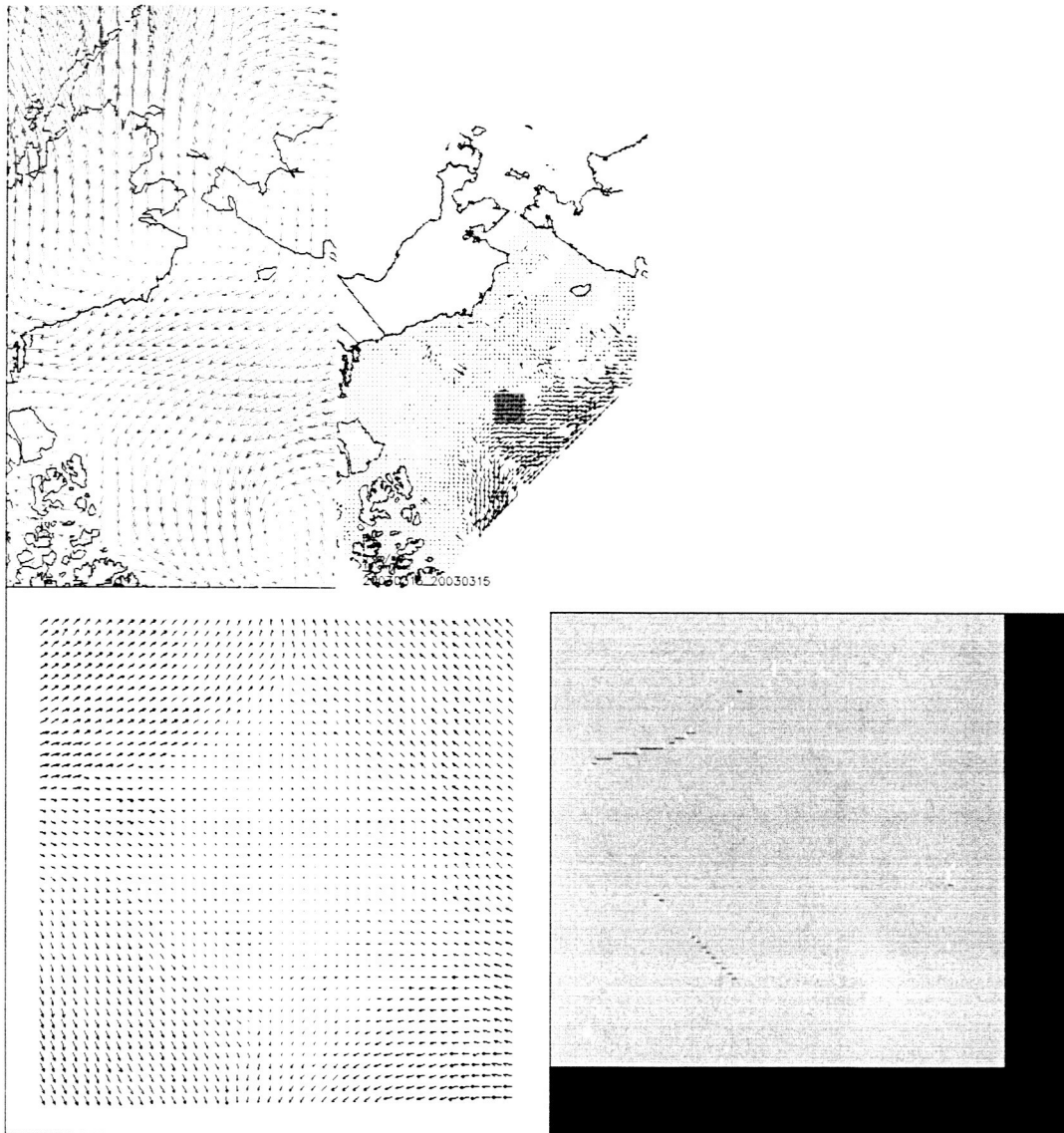
Figure 34. Case for 13-14 March 2003, with strong convergence. The SAR motions in the upper left suggest a plate in the center of the image that is responding differently than the surrounding ice, resulting in some shear and potential open water production as shown in the synthetic lead image on the lower right.

Finally, in Figure 35, we include another case where the plate motion of the ice pack as seen in the SAR data is very obvious. Previous investigators have pointed out this apparent plate configuration. Our work demonstrates that this plate nature translates into potential open water production even when the overall motion field is convergent.
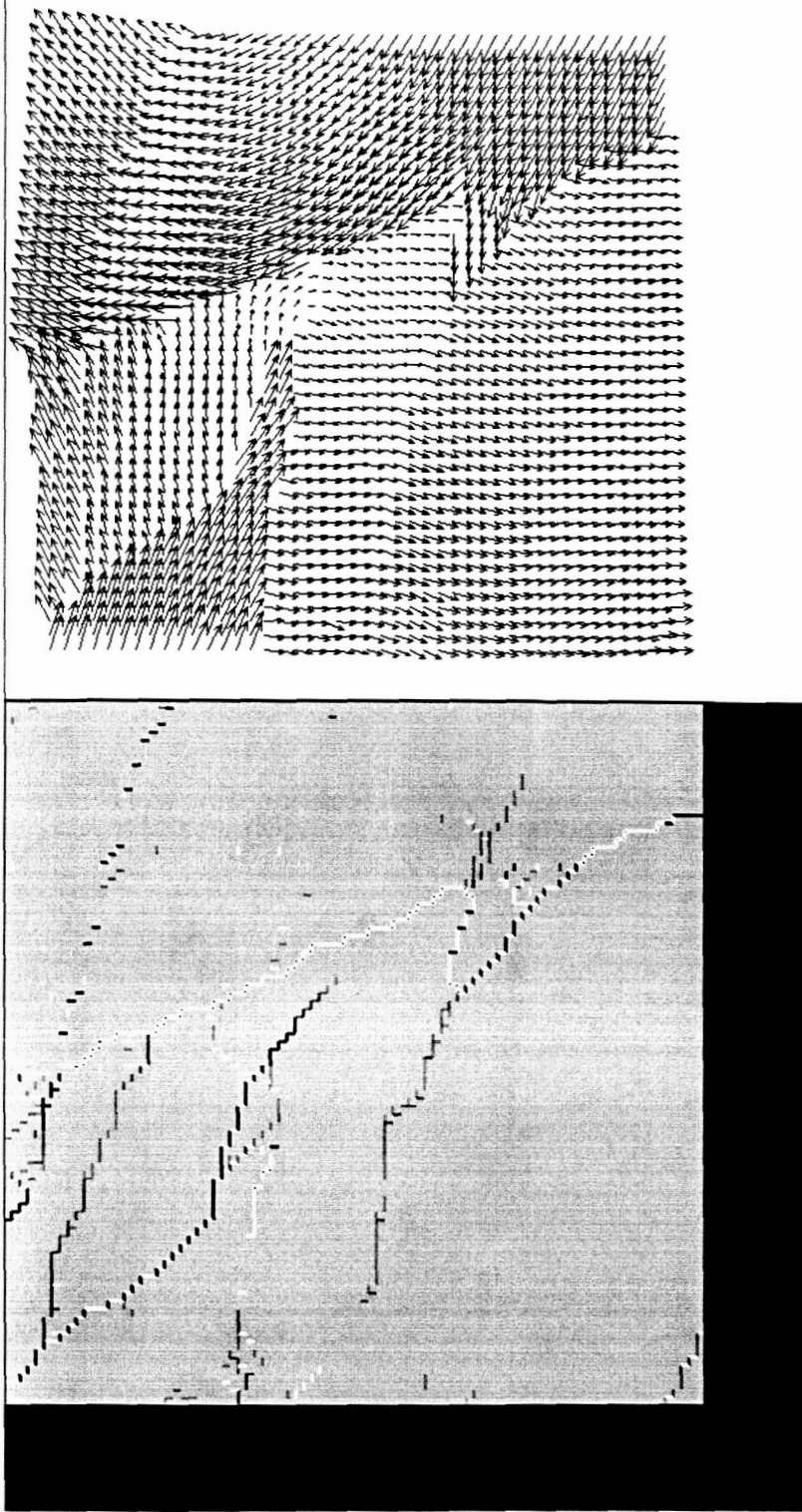
Figure 35. RADARSAT-derived ice motion for 6-7 April 2003 (top) and resulting synthetic lead image (bottom). In this case, the plate-like patterns in the ice movement are readily apparent, as is the way this plate motion translates into areas of open water and ridging.

3.8 Parameterizations of Lead Properties Based on Ice Conditions

As noted earlier, since large-scale climate models do not have the capability to explicitly simulate aspects of lead conditions such as ice formation processes, lead width and lead orientation that have been shown to significantly affect flux calculations. Our approach is to investigate statistical relationships that might link these detailed lead conditions to properties that the models can simulate, such as large-scale ice motion, ice concentration, ice thickness and ice age. Toward this end, we compiled a variety of ice data sets depicting these properties. In particular, we used ice motion data to calculate ice residence times in the Arctic and Southern Ocean. Our intent was to relate lead properties to ice age using these data sets.

3.8.1 Ice Age Estimation

In an effort to quantify the behavior of old ice and first-year ice in the Arctic, we have carried out an initial study of the potential of combining remotely sensed ice motion and ice extent to provide an alternative approach to estimating temporal ice age evolution for late 1978 through the present. As part of the NASA/NOAA Pathfinder program, we used a combination of data from the Scanning Multichannel Microwave Radiometer (SMMR), the Special Sensor Microwave/Imager (SSM/I), and the optical and thermal channels of the Advanced Very High Resolution Radiometer (AVHRR) to first compute the daily movement of Arctic sea ice from sequential satellite images using the Maximum Cross Correlation (MCC) method. These were then blended with International Arctic Buoy Program (IABP) buoy motions for the period from 1978 to 2003.

Sea ice extent was estimated from the passive microwave satellite imagery using the NASA Team algorithm. Treating areas with more than 40% ice concentration as ice covered, we estimated the residence time of a segment of sea ice by advecting ice between each approximately 12 km square grid cell with the appropriate daily sea ice vectors. The 40% ice concentration threshold is a conservative value chosen to minimize the introduction of errors associated with use of the ice concentration algorithm.

The procedure operates as follows. Ice that is present at the beginning of September each year, having survived the summer melt period, is considered old ice. Each 12 km cell of this old ice is then advected throughout the time period, in this study until March 2003, yielding maps consisting of advected old ice for each year. The ice is advected at 1-week intervals using weekly mean velocity fields. An ice age map for a given time step is generated by first treating the current ice extent as first-year ice. The previous year's old ice is then mapped onto the study domain for the current time step, with the assumption that if old ice is present at a grid location in the previous time step, then the ice at this location will be the old ice from this step, rather than first-year ice. This process is then repeated for each of the previous years' advected old ice. Ice is lost whenever an ice cell is advected outside the Arctic Basin domain or when ice concentration decreases below 40% at a grid cell. The position of each ice grid cell is calculated at sub-grid resolution throughout the time period. The process was initialized using the ice extent from November 1978 (the start of the SMMR data record). Therefore, any ice present at that

time that might have been older than second-year ice was nevertheless assigned to the second-year ice category.

Ice that diverged to yield open water area during autumn through spring and was then subsequently shown to have refrozen was assigned to the first-year ice category. Ice of any age that flowed out primarily via Fram Strait was considered to be lost from the Arctic Basin. Convergence of ice will also appear as lost ice area. To simplify the processing, any ice older than 4 years was placed in a "≥ 4-year ice" class.

Using ice extent instead of concentration to define ice-covered area will tend to overestimate the amount of old ice at the beginning of autumn. This occurs since divergence within the ice pack during the summer months will yield areas of new ice at the beginning of September, whereas we treat such areas as old ice. The use of the 40 percent concentration threshold for the ice extent will thus slightly overestimate the amount of old ice present at the beginning of September. Hence, any negative trends in old ice area can be considered to be a conservative underestimate.

With this approach, we were able to infer the residence times of the sea ice and to estimate the areal coverage of each age class. While relatively straightforward to implement, the procedure is somewhat difficult to visualize. The approach is not an ice model in the conventional sense, but in concept might be considered a heavily data-driven model that uses observed ice motion to describe ice dynamics, with observed ice extent representing some of the thermodynamical processes.

Previous studies that have examined trends in sea ice cover based on passive microwave data relied on microwave emission at multiple frequencies to estimate total ice concentration and fraction of old ice (typically referred to as "multiyear" ice by the remote sensing community). While these algorithms are fairly robust, they nevertheless are affected by secondary factors that modify microwave emission in ways that affect ice concentration and type estimation. For example, an increase in melt pond fraction yields apparent decreases in ice concentration, while changes in snow cover could affect estimates of old ice fraction due to effects on the spectral gradient between the 37 GHz and 18 or 19 GHz microwave channels used to estimate old ice concentration. Furthermore, changes in atmospheric conditions such as an increase in atmospheric water content, such as might be expected with the warming of the Arctic troposphere yields a false decrease in old ice fraction using typical algorithms (7). While none of these sources of error are likely to be sufficient individually to account for the observed magnitude of the microwave-derived changes in ice cover seen in the studies noted above, the degree to which multiple error sources might combine to affect traditional calculation methods has not been determined.

To further illustrate these changes, we take a cross section of ice age class across the central Arctic from Banks Island to the Kara Sea (Fig. 36). This cross section shows the ice age class for each year, and illustrates the overall decrease in ice age over the time period. Events such as the large decrease in old ice in 2002 are consistent with other

observations (10) and warrant further examination that might provide insights into the physical processes at work.
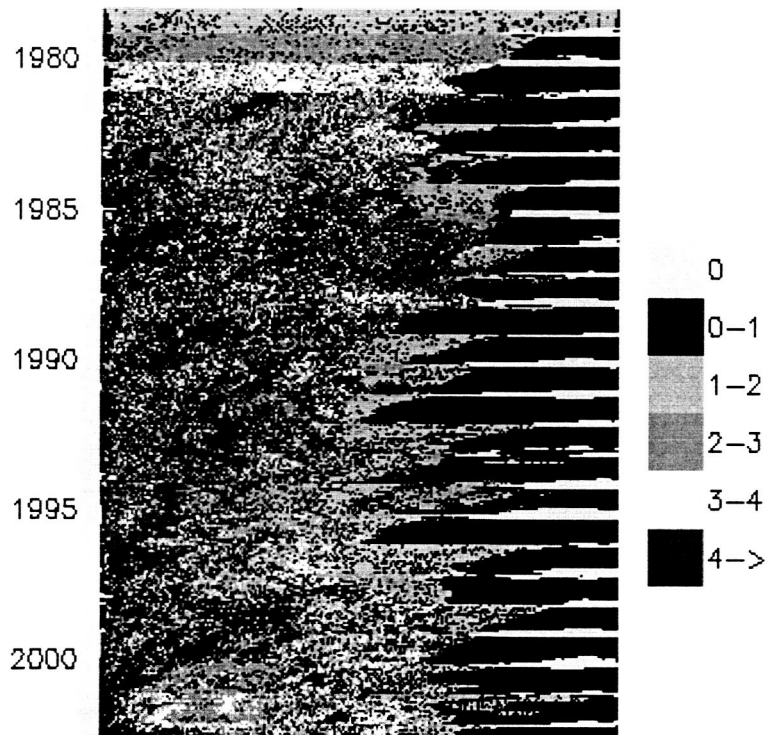

Fig. 36 Cross section of ice age classes extending along a transect across the Arctic from the Canadian Archipelago to the Kara Sea.

To further demonstrate potential applications of these results, Fig. 3 shows the drift of the Surface HEat Budget of the Arctic (SHEBA) ice camp during October 1997-September 1998, plotted on an animation of the estimated ice ages and multiyear ice concentrationsfor that time period. This map suggests that the camp was deployed adjacent to old ice to the west and north, with a mixture of first-year and second-year ice to the south and east. Reports of ice conditions during the initial ice-breaker transit (essentially due north from the ice edge to the camp location shown on week 39 in the top panel in Fig. 37 indicate that the ship sailed through a weak and variable ice cover, with the camp finally deployed within thicker, heavier ice. This description is in keeping with the ice ages shown in this short animation. The relationship of the camp location to ice ages in the general area persists throughout the year of drift, with the camp remaining adjacent to a band of the oldest ice. In this regard, the ice age maps may provide guidance for extrapolating conditions seen at the SHEBA camp to ice conditions elsewhere in the western arctic, and assessing the suitability of SHEBA-based model parameterizations for other areas of the ice pack.

Also shown in this figure is the corresponding animation of multiyear ice concentration as estimated by the NASA Team algorithm. Some basic similarities between the top and bottom panels are apparent, as well as some areas of discrepancies such as the transient appearances and disappearances of patches of multiyear ice in the southern Beaufort Sea in the SSM/I product. This suggests ways that the two data sets might be combined to

help reduce some of the well-recognized ambiguities in microwave-derived ice age classifications.
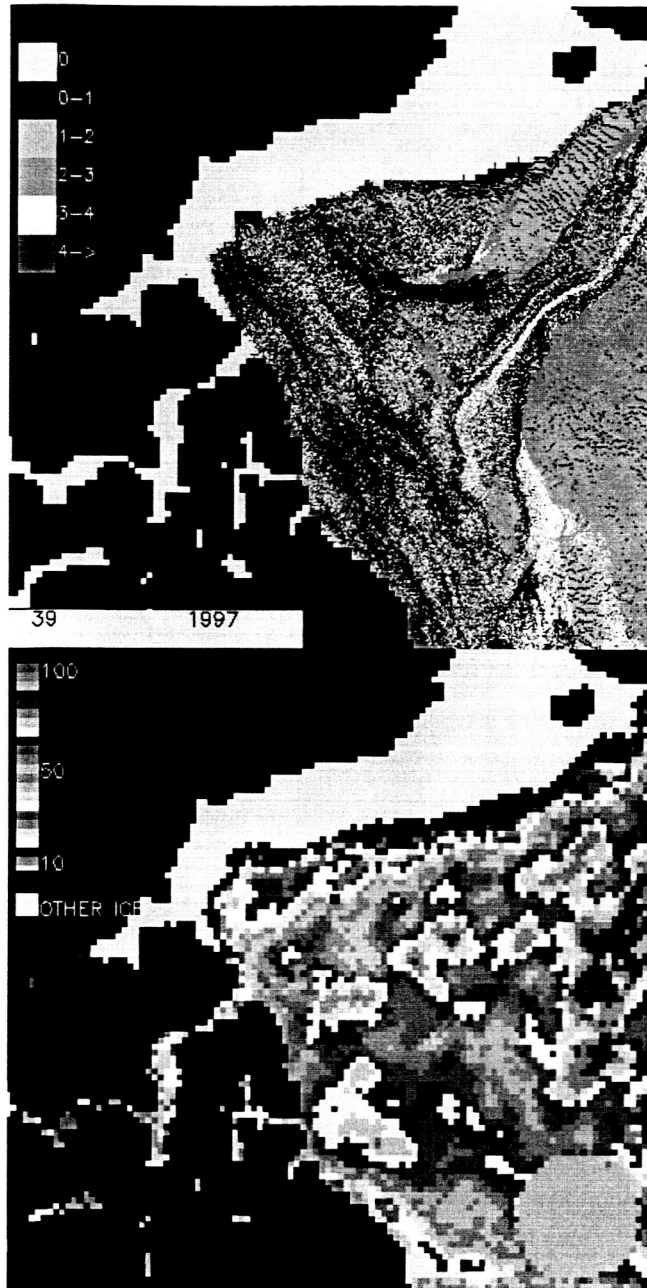

Figure 37. Estimated ice age for 1 Oct. 1997. The SHEBA camp location is indicated by the black square. SSM/I-derived multiyear ice concentration is shown in the lower panel.

Consistent with other results showing considerable divergence and new ice formation during November 1997-January 1998 near the SHEBA camp (8) the proportion of first-year ice in the vicinity of the camp is seen to increase substantially during week 43 (1997) through week 3 (1998), as this portion of the ice pack drifts to the east.

3.9 Modeling Activities

Modeling work focused on additional sensitivity studies of the lead flux model, including application of the model to a particular lead observed during SHEBA (research supported jointly by SHEBA NSF funding). This lead is of particular interest for this project since it represents the only case for which we have a combination of in situ measurements, surface-based photographs and observations, aircraft data, and frequent RADARSAT coverages. Of particular relevance to our project is the demonstrated sensitivity to fetch, surface ice conditions within the lead, and the effects of surface conditions on solar absorption. Using the lead model, testing was also done to estimate the effects of leads on areally averaged fluxes when detailed information on lead widths and ice thickness is available. For this, submarine sonar data were used as a proxy for lead width information. This work demonstrated that lead-flux parameterizations using basic lead and ice information such as that potentially obtainable from satellite data are feasible and likely to be effective within climate models.

Other modeling activities supported in part by this grant included tests of fetch-dependent parameterizations and further refinements of the ice model used for stand-alone simulations and as part of ArcSyM. For this testing, we used an earlier version of our stand-alone sea ice model that includes a parameterization to adjust turbulent flux transfer coefficients as a function of fetch. We plan to incorporate this and other parameterizations that are dependent on lead characteristics into a version of the NCAR Community Sea Ice Model (CSIM) that is under development by NCAR for use within the Community Climate Model. Implementation of CSIM at C.U. is being carried out through other funding.

3.9.1 Heat Flux Sensitivity Studies.

Our original plan for flux calculations was to use a detailed model developed by co-principal investigator Afshan Alam. Dr. Alam has left the research field for an extended period, and is unavailable to pursue this aspect of the work with her model. To accommodate this, we have taken two steps. First, Dr. Alam provided us with her code and instructions regarding its use. Secondly, we decided to use a model of intermediate complexity developed by us, and which was used previously to study the effects of lead fetch and atmospheric boundary layer conditions on turbulent fluxes. This model takes into account the effects of lead fetch and atmospheric stability on fluxes, and allows for the specification of a range of ice and snow thicknesses within leads and on thick ice. An zero-layer thermodynamic ice model is used to calculate skin temperatures and fluxes given user-supplied air temperature, wind speed, humidity, and downwelling atmospheric radiative fluxes. Since our interest is in leads, the zero-layer model is suitable for the linear temperature profile typical of ice less than 0.5 m thick. We modified this 1-dimensional model into a 2-D formulation, and re-wrote the code to improve its efficiency for this project. Inputs were expanded to include grids of estimated ice and snow thickness (for thick ice and for leads), lead/not-lead mask, and lead fetch.

With this model, we are able to test the results of different lead mapping methods and lead parameterizations on turbulent fluxes. The flux model was applied to the March 2000 test case to assess the effects, in terms of fluxes, of lead mapping using different sensor resolutions. NCEP meteorological fields were used as input. The flux model was also applied to each of the AVHRR images in January 1998 case study. Here, field - measured meteorological data were used as input. The wavelet-transform fusion example shown above was also used as a test case.

The first step in applying the flux model is to assign an estimated ice thickness to each pixel. This was done based on manual interpretation of skin temperature, backscatter, or fusion color images, or ice type as mapped by the maximum likelihood classifier. Ice and snow thicknesses were assigned based on typical values for these locations or, for the SHEBA case, on field measurements. A brief summary of the results to date for this initial flux modeling are given below. We are in the process of preparing a journal manuscript that provides more detail on these flux experiments. We should also note that we still intend to take advantage of the Alam models, which are able to make use of additional lead information such as type of ice and presence of waves - characteristics that can to some degree be extracted from the image composites we are working with.

As mentioned, the first step in the flux modeling is assigning ice thicknesses to the area of coverage. Since as discussed above, the lead classification differs based on input (SAR, AVHRR temperatures, fused imagery, etc.), the thickness "maps" will vary as well. This will then translate directly into differences in fluxes. Figure 38 compares the ice thickness maps and resulting sensible heat fluxes using SAR backscatter and AVHRR skin temperatures as input (see examples in Figures 25 and 26). The ability of the AVHRR data to identify warm, presumably thin, ice yields a greater fraction of estimated thin ice, resulting in more pixels with larger heat fluxes. Using these data as input, a suite of experiments was carried out to test the sensitivity of the estimated fluxes to several scenarios. One experiment tested the significance of the ability to define leads with thin ice versus dividing the image into "thick ice" and "open water". The former is intended to represent the potential of the newer generation of climate-type ice models that include multiple thickness categories, while the "thick ice/open water" binary classification is comparable to that used in older sea ice models, most regional climate models, and all or nearly all GCMs. A second experiment examined the effects of using a stability-adjusted turbulent flux transfer coefficient versus a fixed, pre-defined coefficient. Another experiment studied the effects of allowing the flux transfer coefficient to vary with lead fetch. As with ice thickness, these choices are typical of the types of parameterization options used in climate models.
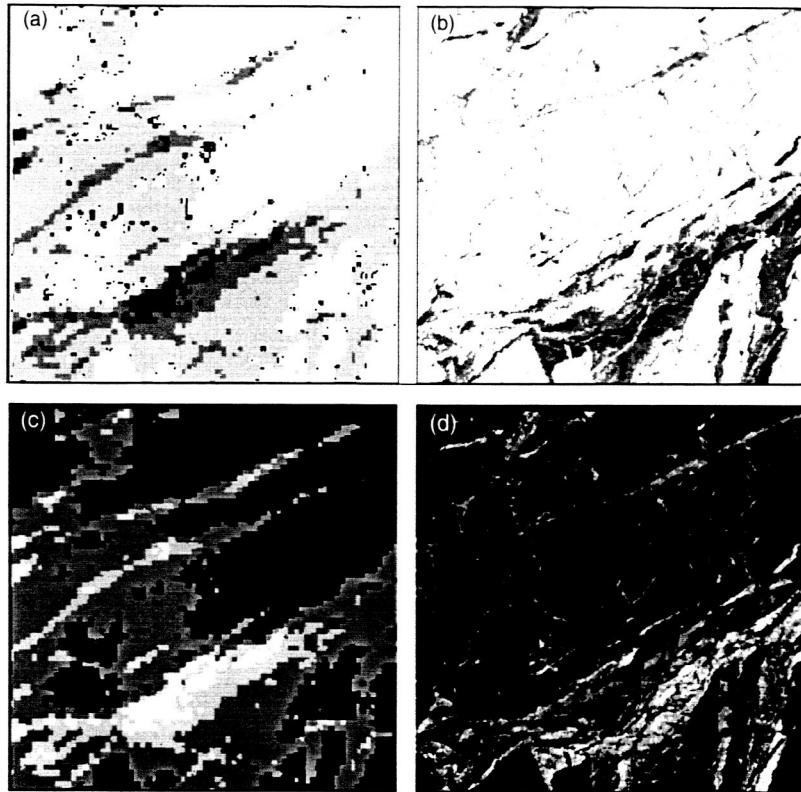
Figure 38. Ice thickness maps estimated from SAR (a) and AVHRR skin temperature (b). Resulting sensible heat flux field modeled using (a) and (b) as input (shown in (c) and (d), respectively.)

The effects on fluxes of image types as they affect ice classification, and on the ability of the model to make use of more detailed ice-pack information than just a lead/thick ice distinction, is further illustrated in Figure 39. We are also examining the variability in fluxes over time, using the SHEBA January case. Figure 40 shows a sequence of flux fields estimated for this case, using the AVHRR skin temperature images (shown earlier in Figure 25) to define lead and ice conditions. The mean flux varies considerably from day to day, associated mainly with the changing lead fraction and the ice thicknesses assigned to the leads.
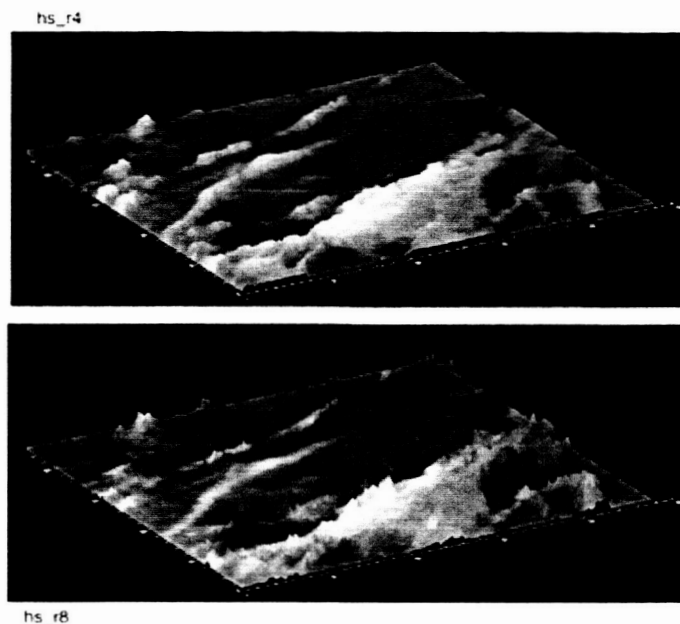
hs_r4

hs_r8

Figure 39. Comparison of fluxes estimated using the AVHRR-derived lead fraction and ice thickness estimates with fixed (top) vs. fetch- and stability-adjusted bulk transfer coefficients (bottom)(for the image area in Figure 12
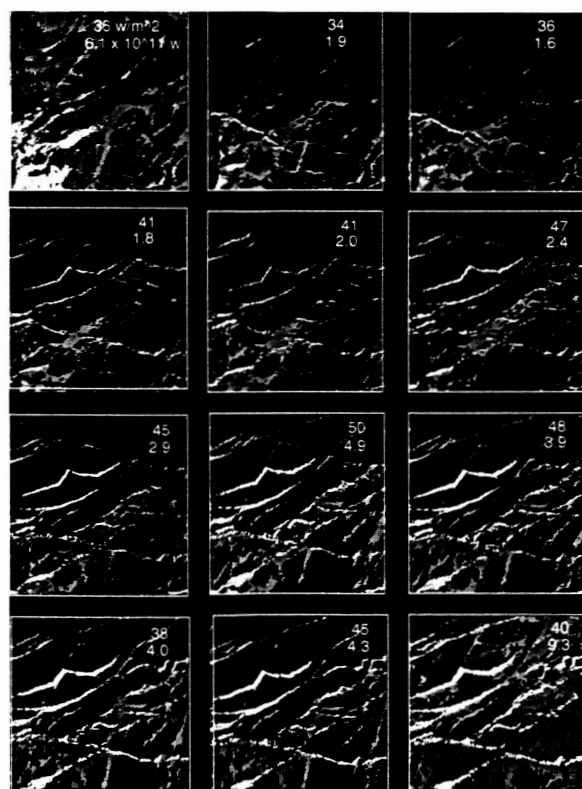

Figure 40. Sensible heat flux fields estimated using the Maslanik flux model for the sequence of images in the January SHEBA case. Values shown in each panel are mean flux (upper value) and total heat output within the image area. Note the changes in the flux fields corresponding to the changes in lead patterns seen in Figure 6.

4.0 Conclusions

The premise of our project is that modeling and remote sensing of sea ice processes have reached a level of maturity where the models require detailed information for testing and refinements, and where such information can now be obtained from multisensor approaches. Given this, the goals of our work were to: (a) refine and test the local-scale parameterizations used within an existing, detailed lead model; (b) identify relationships between the local-scale lead characteristics needed as input to the lead model and large-scale sea ice conditions that can be simulated by climate models; and (c) test the improvement in the climate simulations when these relationships are used to implement the detailed lead flux calculations. A key aspect of the project was the use of RADARSAT data, in concert with a wide range of other data types, to document fine-through coarse-scale characteristics of leads in the context of the types of background ice and atmospheric information that can be simulated by state-of-the-art coupled ice-atmosphere-ocean models such as the Arctic Regional Climate System Model (ARCSyM). Objectives to meet these goals included:

- Derivation of detailed lead conditions for modeling test cases using RADARSAT, aircraft, and other satellite data sets acquired the Surface Heat Budget of the Arctic (SHEBA) period, with additional test cases during the expected RADARSAT/MODIS overlap period in autumn, 2000;
- Use of these data to evaluate the differences in fluxes and ice growth for leads estimated using a new lead model versus estimates obtained using standard bulk formulae;
- Applications of the SAR data and SAR-based products to test and refine the parameterizations and assumptions inherent to the new lead model;
- Identify correlations and relationships between local lead conditions critical for the lead model and larger-scale ice and atmospheric conditions;
- Link these correlations to conditions simulated by large-scale models;
- Demonstrate the improvement achieved by implementing these remote-sensing derived parameterizations within an Arctic climate simulation.
- Carry out a limited comparison of the Arctic-based parameterizations with Antarctic ice conditions to assess how representative such parameterizations are likely to be Southern Ocean simulations.

The bulk of the project activities focused on (a) identification and assembly of multisensor data sets depicting various lead conditions, (b) development and testing of lead processes and parameterizations within the detailed lead model and within a stand-alone ice model destined for use in ARCSyM, and (c) initial studies of relationships between lead characteristics and large scale atmospheric and weather conditions. .

The major (in terms of science results and effort) activities and findings during the project are as follows:

- Investigated a series of AVHRR, MODIS, RADARSAT and AMSR-E image time series to identify large-scale lead patterns.
- Obtained and georeferenced a combined set of SAR, AVHRR, and MODIS for the southern and central Beaufort Sea and the eastern Chukchi Sea.
- Acquired and re-gridded NCEP forcing fields useful for quantifying relationships between atmospheric forcings and lead patterns.
- Generated a similar data set for ice motion, including updates and refinements of AVHRR Polar Pathfinder ice motion fields.
- Used ice concentration and ice motion data to calculate ice residence times (i.e., ice age) for the Arctic and Antarctic and related these ages to lead formation and characteristics.
- Demonstrated that the distribution of ice ages in the Arctic Basin has changed substantially over the last 22 years, with a large decrease in the area of oldest ice.
- Tested a suite of MATLAB software tools for data fusion.
- Tested fusion methods provided by the PCI Geomatica software package.
- Explored data fusion approaches applied composites of AVHRR, MODIS and RADARSAT imagery to extract lead information based on combined optical, thermal and radar characteristics.
- Tested and applied image classifications (maximum likelihood) and data visualization as data fusion approaches as means of extracting a variety of lead parameters.
- Quantified effects of image type and spatial resolution on retrieved lead fractions and conditions.
- Employed a set of software routines to extract "object oriented" lead information such as width, length and orientation useful for comparing to large-scale forcing fields.
- Modified and applied a lead flux model to quantify effects of different input information, lead parameterizations, and transfer-coefficient treatments on turbulent fluxe estimates.
- Tested additional lead flux models capable of providing improved flux calculations given the types of lead information provided by the fusion, classification and object characterization steps listed above.
- Used ice motion fields at various scales to quantify the formation of open water via calculation of "synthetic leads".
- Through the synthetic lead analysis, showed that even in cases of net convergence (i.e., areas where an ice model would produce no open water), RADARSAT-derived ice motion yields some open water production due to the apparent plate-like nature of the ice pack at this fine spatial scale.

5.0 Supported Publications

Fowler, C., W. Emery and J. Maslanik, 2004. Satellite derived evolution of Arctic sea ice age: October 1978 to March 2003, IEEE Trans. Geosci. And Remote Sensing (in press)

Curry, J.A., J. Maslanik, G. Holland, J. Pinto, B. Argrow, S. Drobot, J. Inoue, B. Mulac, G. Tyrrell, M. Gonella, and D. Fowler. 2004. Applications of Aerosondes in the Arctic, Bull. Am. Met. Soc. (in press).

Maslanik, J. and C. Fowler, 2004, Platelike motion of Arctic sea ice – implications for lead production and heat flux estimation (in prep.)